Draft version April 7, 2025
Typeset using LaTeX **twocolumn** style in AASTeX7

Precise Asteroseismic Ages for the Helmi Streams

Christopher J. Lindsay,[1] Marc Hon,[2] J. M. Joel Ong (王加冕),[3,4] Rafael A. García,[5] Dinil B. Palakkatharappil,[5] Jie Yu,[6,7]
Tanda Li (李坦达),[8] Tomás Ruiz-Lara,[9,10] and Amina Helmi[11]

[1] *Department of Astronomy, Yale University, PO Box 208101, New Haven, CT 06520-8101, USA*
[2] *Kavli Institute for Astrophysics and Space Research, Massachusetts Institute of Technology, Cambridge, MA 02139, USA*
[3] *Institute for Astronomy, University of Hawai'i, 2680 Woodlawn Drive, Honolulu, HI 96822, USA*
[4] *Hubble Fellow*
[5] *Université Paris-Saclay, Université Paris Cité, CEA, CNRS, AIM, 91191, Gif-sur-Yvette, France*
[6] *School of Computing, Australian National University, Acton, ACT 2601, Australia*
[7] *Research School of Astronomy & Astrophysics, Australian National University, Cotter Road, Weston, ACT 2611, Australia*
[8] *Department of Astronomy, Beijing Normal University, Haidian District, Beijing 100875, People's Republic of China*
[9] *Departamento de Física Téorica y del Cosmos, Universidad de Granada, 18071 Granada, Spain*
[10] *Instituto Carlos I de Física Téorica y Computacional, Facultad de Ciencias, 18071 Granada, Spain*
[11] *Kapteyn Astronomical Institute, University of Groningen, Landleven 12, 9747 AD Groningen, The Netherlands*

ABSTRACT

The Helmi streams are remnants of a dwarf galaxy that was accreted by the Milky Way and whose stars now form a distinct kinematic and chemical substructure in the Galactic halo. Precisely age-dating these typically faint stars of extragalactic origin has been notoriously difficult due to the limitations of using only spectroscopic data, interferometry, or coarse asteroseismic measurements. Using observations from NASA's Transiting Exoplanet Survey Satellite, we report the detailed asteroseismic modeling of two of the brightest red giants within the Helmi streams, HD 175305 and HD 128279. By modeling the individual oscillation mode frequencies and the spectroscopic properties of both stars, we determine their fundamental properties including mass, radius, and age (τ). We report $\tau = 11.2 \pm 1.6$ Gyr for HD 175305 and $\tau = 12.4 \pm 0.8$ Gyr for HD 128279, consistent with previously inferred star-formation histories for the Helmi streams and the differential chemical abundances between the two stars. With precise ages for individual stream members, our results reinforce the hypothesis that the Helmi streams' progenitor must have existed at least 12 Gyr ago. Our results also highlight that the ages of metal-poor, α-enhanced red giants can be severely underestimated when inferred using global asteroseismic parameters instead of individual mode frequencies.

Keywords: asteroseismology - stars: solar-type - stars: oscillations - Galaxy: halo - Galaxy: formation

1. INTRODUCTION

The ΛCDM cosmological model predicts that our galaxy has grown hierarchically through mergers with smaller satellite galaxies (V. Springel et al. 2005). Observational evidence supporting this scenario comes from the dynamics and compositions of the Milky Way's halo-cluster system, as halo star abundance patterns align with the idea that galaxies build their stellar populations by accreting gas and already-formed stars from lower-mass galaxies (L. Searle & R. Zinn 1978; J. Bland-Hawthorn & P. R. Maloney 2002; P. Richter 2017). The goal of Galactic archaeology is to build a time-resolved picture of the Milky Way's formation, including its early merger events. To that end, the *Gaia* mission (Gaia Collaboration et al. 2016, 2018, 2021) has successfully enabled the detection of kinematically distinct stellar-population structures within the Milky Way as evidence for both minor and major mergers (e.g., C. J. Grillmair & J. L. Carlin 2016; A. Helmi et al. 2018; A. Helmi 2020).

Even though stars accreted in the distant past have since phase-mixed with the Milky Way's stars, dispersing in position and velocity thus blending into the galaxy's overall stellar population, their structure remains preserved in the space of integrals of motion (A. Helmi & P. T. de Zeeuw 2000; A. Helmi 2020; E. Dodd et al. 2023). By combining position and velocity measurements from *Gaia* with stellar abundance data, it is possible to determine a star's progenitor. Progenior identification within the *Gaia* 6D sam-

Corresponding author: Christopher Lindsay
christopher.lindsay@yale.edu

ple has already been carried out (e.g., H. Koppelman et al. 2018; A. M. Price-Whelan & A. Bonaca 2018), revealing numerous structures in the stellar halo, including the Gaia-Enceladus/Sausage which played a major role in forming the Milky Way's inner halo (A. Helmi et al. 2018, and references therein). Both the Gaia-Enceladus Sausage (H. Koppelman et al. 2018) and Sagitarrius streams (R. A. Ibata et al. 1994) form large contributions to the Milky Way's inner halo and also influence the star formation history of the Milky Way (T. Ruiz-Lara et al. 2020). The inclusion of individual elemental abundance measurements reveals that individual streams may have distinct chemical properties indicative of their progenitors' star formation history (e.g., I. U. Roederer et al. 2010; R. P. Naidu et al. 2020; T. Ruiz-Lara et al. 2022b; T. Matsuno et al. 2022; E. Dodd et al. 2023; D. Horta et al. 2023).

While the identification of stellar streams has been greatly invigorated in recent years (A. Bonaca & A. M. Price-Whelan 2025), the exact history of their merging into the Galaxy remains highly uncertain. Traditional approaches for determining the ages of stellar streams applied isochrone fitting, which may be particularly uncertain for red giants (e.g., P. Das et al. 2020). The advent of asteroseismology as a tool for Galactic archeology has provided new prospects for precisely age-dating stellar populations around the Milky Way, including members of cold stellar streams.

Nearly all asteroseismic studies involving Galactic archaeology, however, rely on two 'global' measurements of the time-resolved oscillation spectrum of low-mass red giants. These are the large frequency spacing ($\Delta\nu$) between successive radial modes and the frequency at maximum oscillation power $\nu_{\max}$ (H. Kjeldsen & T. R. Bedding 1995; S. Basu & W. J. Chaplin 2017). Because the quantity $\Delta\nu$ scales approximately with the square root of the stellar density while $\nu_{\max}$ scales with the star's surface gravity and temperature, they provide unique constraints on red giant radii, masses, and subsequently ages when combined with temperature measurements.

However, there has been mounting evidence that the use of global asteroseismic measurements for metal-poor stars — including stars in stellar streams — significantly overestimates masses (and subsequently underestimates ages). This discrepancy is not observed when individual oscillation modes are fitted to stellar models, which remains the gold standard for asteroseismic analyses (D. Huber et al. 2024). Global asteroseismology has been applied to remnant stars born in external galaxies (C. C. Borre et al. 2022) but to date, detailed asteroseismic modeling has not yet been performed for any star that is firmly established to be a member of a stellar stream. The detailed asteroseismic modeling of ν Indi (W. J. Chaplin et al. 2020) provided an exemplary study for age-dating Gaia-Enceladus merger, though the star is thought to have been born locally within our Milky Way.

In this work, we study two firmly established members of the Helmi streams: red giants HD 175305 and HD 128279. The Helmi streams are the remnants of a disrupted dwarf galaxy with an estimated stellar mass of about $10^8 M_\odot$, believed to have merged with the Milky Way approximately 5 to 8 Gyr ago (A. A. Kepley et al. 2007; H. Koppelman et al. 2018; R. P. Naidu et al. 2022; H. C. Woudenberg & A. Helmi 2024). Having many stream members within several kiloparsecs to the Sun, the Helmi streams were among the earliest kinematic substructures associated with an accretion event (A. Helmi et al. 1999). It is this proximity which provides us with the novel opportunity to perform the detailed asteroseismic modeling of the two red giants, which are thought to be of extragalactic origin.

We report the spectroscopic and asteroseismic data for the two target stars in section 2 and describe our asteroseismic modeling methods in section 3. The modeling results are detailed in section 4 and implications of these results are discussed in section 5.

2. TARGET STARS

The spectroscopic and global asteroseismic properties of the target stars, HD 175305 and HD 128279 are listed in Table 1 along with the data sources. HD 175305 is a metal poor ([Fe/H] = -1.35) and moderately alpha-enhanced ([α/Fe] = 0.23) red giant star in the Transiting Exoplanet Survey Satellite's (TESS G. R. Ricker et al. 2015) Northern Continuous Viewing Zone. It is also a Gaia-benchmark star, with its elemental abundances and fundamental properties studied extensively using spectroscopy (e.g., M. N. Ishigaki et al. 2012; Abdurro'uf et al. 2022) and interferometry (I. Karovicova et al. 2020; C. Soubiran et al. 2024). HD 128279 is also a red giant star, but is located closer to the ecliptic. Compared to HD 175305, HD 128279 is more metal poor ([Fe/H] = -2.17), more alpha enhanced ([α/Fe] = 0.30), and less luminous. The luminosity values we report for both HD 175305 and HD 128279 were calculated using the SED EXplorer spectral energy distribution fitting pipeline (SEDEX J. Yu et al. 2023).

2.1. *Kinematics*

Both HD 175305 and HD 128279 were first identified as members of the Helmi streams using kinematic measurements from the *Hipparcos* satellite (T. C. Beers et al. 2000; M. Chiba & T. C. Beers 2000), forming part of a distinct clustering in angular momentum ($L_z - L_\perp$) space. These two stars have maintained their stream membership in the presence of more comprehensive 5-D and 6-D kinematic data from the *Gaia* mission (H. H. Koppelman et al. 2019; S. S. Lövdal et al. 2022; T. Ruiz-Lara et al. 2022b; E. Dodd et al. 2023). To illustrate this, we present the kinematic signatures of the two stars based on Gaia DR3 data in Figure 1. The left panel shows the sample of kinematically selected Halo stars from

Table 1. The stellar parameters of the target stars analyzed in this study, HD 175305 and HD 128279.

	HD 175305		**HD 128279**	
	Value	Source	Value	Source
TIC ID	335965870	TESS Input Catalog*	13727	TESS Input Catalog*
Gaia G Magnitude	6.96	*Gaia* DR3‡	7.82	*Gaia* DR3‡
Effective Temperature (K)	5036 ± 200	M. N. Ishigaki et al. (2012)	5328 ± 200	M. N. Ishigaki et al. (2012)
Luminosity ($L_\odot$)	33.1 ± 3.0	This work	11.1 ± 1.7	This work
Parallax (mas)	6.41 ± 0.01	*Gaia* DR3‡	7.63 ± 0.03	*Gaia* DR3‡
[Fe/H] (dex)	-1.35 ± 0.15	M. N. Ishigaki et al. (2012)	-2.17 ± 0.12	M. N. Ishigaki et al. (2012)
[α/Fe] (dex)	0.23 ± 0.05	M. N. Ishigaki et al. (2012)	0.30 ± 0.05	M. N. Ishigaki et al. (2012)
$\Delta\nu$ (μHz)	5.89 ± 0.01	This work	15.87 ± 0.05	This work
$\nu_{\max}$ (μHz)	52.17 ± 0.37	This work	189.10 ± 0.52	This work

* K. G. Stassun et al. (2019)

‡ Gaia Collaboration et al. (2021)

E. Dodd et al. (2023) in energy (E) - angular momentum (L_z) space with E indicating the total orbital energy of the halo stars (more bound orbits have more negative energies) and L_z representing the rotational component of the star' orbit about the galactic center. The right panel of Figure 1 shows the same sample of stars in velocity space, V_z is velocity out of the plane of the galaxy while V_x is velocity in the direction from the Sun to the galactic center. In both panels, the kinematics of HD 175305 and HD 128279 are consistent with the identification of Helmi stream members by E. Dodd et al. (2023) in blue.

H. C. Woudenberg & A. Helmi (2024) pointed out that the collection of Helmi streams stars shown in Figure 1 and Figure 2 can be split into two separate clumps in ($L_z, L_\perp$) space. Figure 2 shows that HD 175305 (marked with a dark red star symbol) is a member of the high-$L_\perp$ grouping while HD 128279 (marked with a purple star symbol) is a member of the low-$L_\perp$ clump. HD 175305 and the other high-$L_\perp$ stars have larger z-velocities (V_z values in the right panel of Figure 1). Within the high-$L_\perp$ clump within the Helmi streams, previous work has identified a part of the Helmi streams that is significantly less phased mixed, dubbed the subclump in H. C. Woudenberg & A. Helmi (2024). We note that HD 175305 and HD 128279 are not identified as members of the subclump.

2.2. *Asteroseismic Mode Determination*

The multiple sectors of TESS light curves for both our target stars were combined and corrected for systematics. The light curve for HD 175305 was generated using the MIT Quick-Look Pipeline (QLP; C. X. Huang et al. 2020a,b; M. Kunimoto et al. 2021, 2022), which provides sufficient precision for observing giant star oscillations (M. Hon et al. 2021). We used QLP lightcurves from TESS sectors 14-26, 41, 47-51, 53-60, and 73-74 that were processed further using the PYTADACS (Python for Tess Astroseismic and DynAmiC Studies) pipeline (García et al. in prep). The pipeline stitches together contiguous light curve segments spaced further than 3 consecutive sectors apart and performs two iterations of σ-clipping. The first iteration removes all flux measurements deviating further than 10σ of the light curve's mean flux, while the second iteration removes (from the original light curve), flux measurements deviating further than 4σ from the data smoothed with a median filter of 1-day width. Next, the light curve is binned into a regular grid with a 30-minute cadence using the nearest neighbor resampling algorithm with the slotting principle (P. Broersen 2009), as described in R. A. García et al. 2014, 2024. Finally, the light curve is high-pass filtered using a 5-day triangular filter. The effect of the gap removal prescription applied in the lightcurve preparation we used was studied in L. González-Cuesta et al. (2023).

We used the lightcurve generated by the TESS Science Processing Operations Center pipeline (SPOC; J. D. Twicken et al. 2016; J. M. Jenkins 2017) for HD 128279. Though HD 175305 does not have SPOC light curves, we used SPOC data for HD 128279 because they generally preserve flux variability better for bright red giants (M. Hon et al. 2022).

The light curves of both target stars were analyzed for stellar oscillations using the TACO (Tools for Automated Characterization of Oscillations) code (N. Themeßl et al. 2020). The global asteroseismic parameters, $\Delta\nu$ and $\nu_{\max}$, we report for HD 175305 and HD 128279 in Table 1 were calculated using TACO by first calculating a power density spectrum (PSD) from the light curve, dividing out the background component from convective granulation and white noise background, and finding the frequency of maximum oscillation power ($\nu_{\max}$). We show the background-subtracted power spectral density for HD 175305 and HD 128279 in the left panels of Figure 3 and Figure 4 respectively.

Peaks are then identified from the PSD by applying a Mexican-hat wavelet-transform based algorithm iteratively

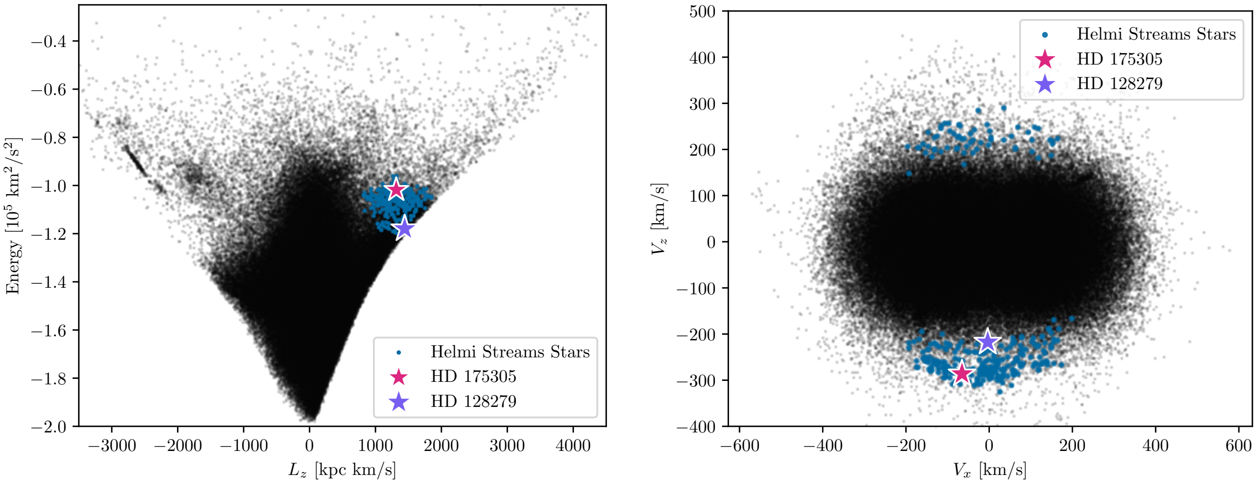

Figure 1. Black points show the kinematically selected Halo star sample from E. Dodd et al. (2023) in energy versus the L_z space (left panel) and V_z versus V_x space (right panel). The blue points in both panels show the stars associated with the Helmi streams (E. Dodd et al. 2023).

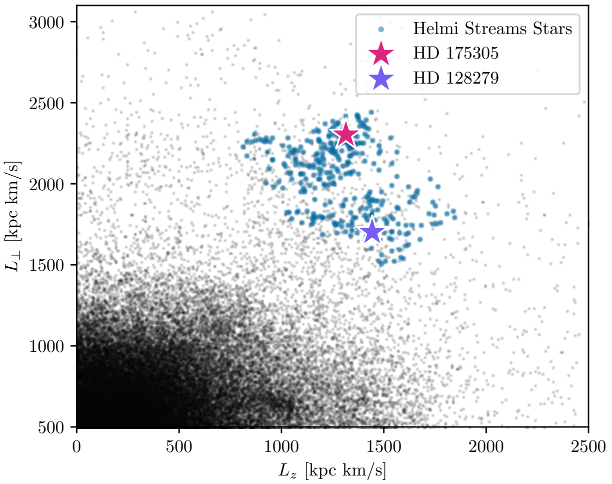

Figure 2. Black points show the kinematically selected Halo star sample from E. Dodd et al. (2023) in $L_\perp$ versus the L_z space (left). The groupings of stars associated with the Helmi streams and our target stars are marked with blue points and star symbols respectively. HD 175305 (dark red star) and HD 128279 (purple star) are members of the high $L_\perp$ and low $L_\perp$ clumps described in H. C. Woudenberg & A. Helmi (2024) respectively.

to find resolved peaks, which are then fitted with Lorentzian functions. The $\ell = 0$ and $\ell = 2$ modes are identified by using the universal pattern for solar-like p-mode oscillations of the same angular degree, $\nu_{n_p,\ell,m} \sim \Delta\nu(n_p + \frac{\ell}{2} + \epsilon_p)$, where $\Delta\nu$ is the large frequency separation, ϵ_p is a phase term, and n_p, ℓ, and m are the p-mode radial order, angular degree, and azimuthal order respectively (M. Tassoul 1980). $\Delta\nu$ is identified by TACO using the frequency spacing between consecutive radial ($\ell = 0$) p-modes. For the peaks not identified as $\ell = 0$ or $\ell = 2$ modes, TACO identifies them as dipole modes ($\ell = 1$). The mode frequencies, mode frequency errors, and angular degrees for HD 175305 and HD 128279 are reported in Table 2 and Table 3 respectively. The dipole ($\ell = 1$) errors determined by TACO for HD 175305 were multiplied by 10 before being used in our modeling since the errors directly from TACO for the HD 175305 dipole modes were a tenth of the errors on the radial and quadrupole modes. Note that the mode frequencies were corrected for stellar line-of-sight Doppler velocity shifts following G. R. Davies et al. (2014) using radial velocities from GAIA DR3 (-184.08±0.12 km/s for HD 175305 and -75.68±0.14 km/s for HD 128279, Gaia Collaboration et al. 2021).

The mode frequencies are visualized using frequency échelle diagrams in the right panels of Figure 3 and Figure 4 for HD 175305 and HD 128279 respectively. The background power échelle diagrams are constructed following G. Grec et al. (1983), by splitting a star's oscillation power spectrum into chunks of width $\Delta\nu$, then stacking these chunks in order of increasing frequency. The lower $\Delta\nu$ value and denser dipole $\ell = 1$ mode spectrum in HD 175305's échelle diagram indicates that HD 175305 is more evolved compared with HD 128279, although the presence of excess dipole modes compared with the number expected from the the p-mode asymptotic relation confirm that both stars are evolved. We further discuss the evolutionary state of HD 175305 in subsection 5.4.

3. ASTEROSEISMIC OPTIMIZATION

In our modeling of HD 175305 and HD 128279, we used the effective temperature, [Fe/H], and [α/Fe] measurements from M. N. Ishigaki et al. (2012) listed in Table 1 along with luminosities and the individual oscillation mode frequencies tabulated in Table 2 and Table 3. The asteroseismic optimization pipeline developed for this project employs the stellar evolution code MESA (Modules for Experiments in Stellar

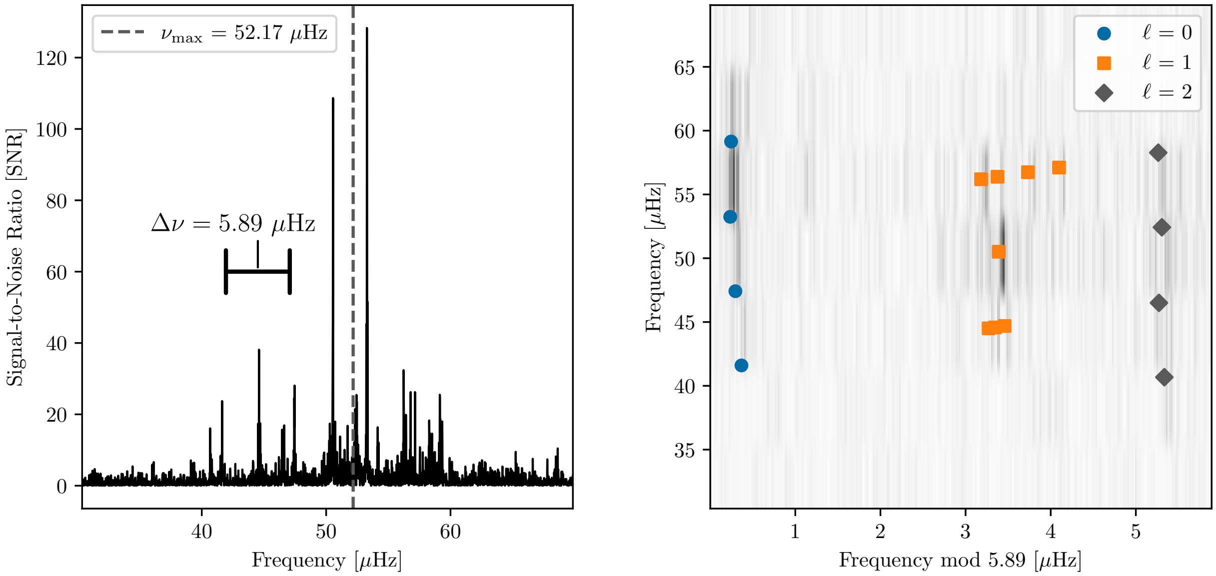

Figure 3. HD 175305 background-subtracted power spectral density (left) and power échelle plot (right). The markers in the power échelle plot show the observed mode frequencies determined using TACO (N. Themeßl et al. 2020).

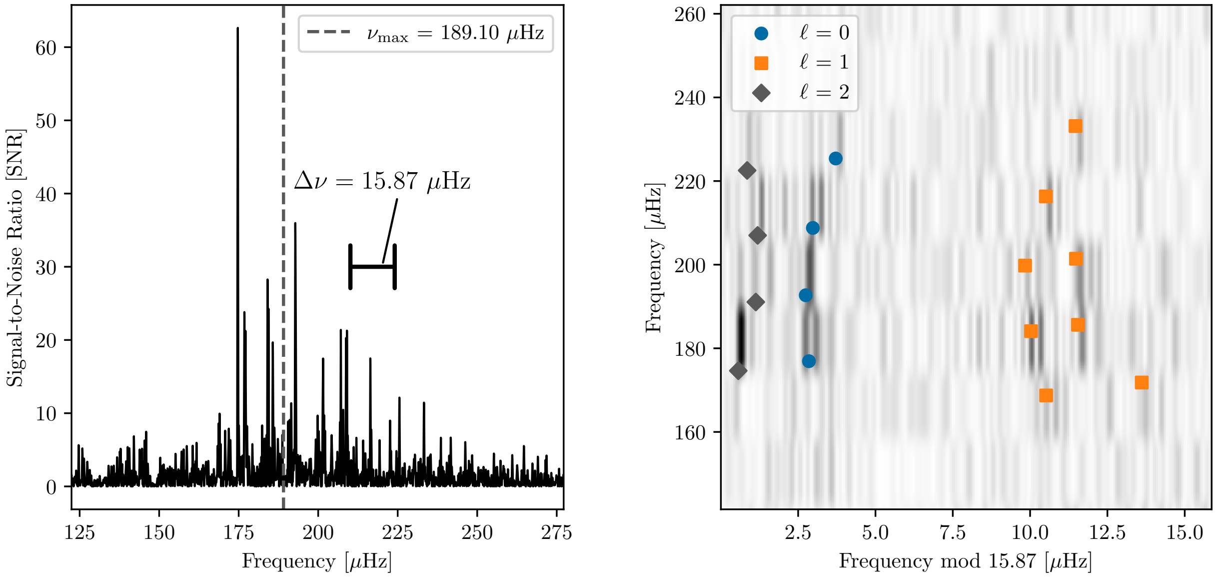

Figure 4. HD 128279 Background-subtracted power spectral density (left) and power échelle plot (right). The markers in the power échelle plot show the observed mode frequencies determined using TACO (N. Themeßl et al. 2020).

Astrophysics B. Paxton et al. 2011, 2013, 2015, 2018, 2019; A. S. Jermyn et al. 2023) and the differential evolution algorithm implemented in P. R. Mier (2017) in order to perform on-the-fly stellar modeling and find stellar model parameters that minimize a cost function taking into account the models' match to the spectroscopic and asteroseismic observables. The parameters we vary are initial mass (M_0, initial helium mass fraction Y_0, initial metallicity ([Fe/H$_0$]), and convective mixing length ($\alpha_{\rm mlt}$). Using `yabox` allows for derivative-free minimization of a cost function, which is evaluated for different combinations of the initial mass, metal abundance, helium abundance and convective mixing length in the steps detailed in Appendix A. The model cost function is similar to that defined in C. J. Lindsay et al. (2024) and incorporates the fit to the spectroscopic observables as well as the fit between the surface corrected model mode frequencies and the observed frequencies (W. H. Ball & L. Gizon 2014) and the magnitude of the surface correction (Y. Li et al. 2023). The

Table 2. Observed Mode Frequencies for HD 175305 determined using the Tools for Automated Characterization of Oscillations (TACO) Code (N. Themeßl et al. 2020).

Angular Degree (ℓ)	Frequency (μHz)	Error (μHz)
2	40.67	0.02
0	41.60	0.02
1	44.50	0.04
1	44.57	0.02
1	44.69	0.01
2	46.50	0.04
0	47.42	0.01
1	50.51	0.02
2	52.43	0.04
0	53.25	0.01
1	56.19	0.01
1	56.38	0.01
1	56.74	0.03
1	57.11	0.01
2	58.28	0.04
0	59.15	0.03

Table 3. Observed Mode Frequencies for HD 128279 determined using TACO.

Angular Degree (ℓ)	Frequency (μHz)	Error (μHz)
1	168.72	0.20
1	171.81	0.11
2	174.63	0.02
0	176.92	0.10
1	184.10	0.08
1	185.62	0.06
2	191.07	0.22
0	192.69	0.05
1	199.78	0.21
1	201.42	0.05
2	207.00	0.14
0	208.78	0.13
1	216.32	0.07
2	222.53	0.08
0	225.39	0.06
1	233.15	0.06

magnitude of the surface correction is downweighted compared to the other components of the cost function and was only taken into account in order to downweight models with very large surface corrections. We note that our analysis and the work of Y. Li et al. (2023) used differet versions of MESA but the same atmospheric boundry condition.

The minimization process continues for a set number of iterations (40 iterations, 840 cost function evaluations) and the minimum output of the cost function through all the evaluations is taken as the best-fit track, with the model corresponding to the minimum χ^2_{total} value along the track being the best-fit model. The number of iterations was chosed based on the number of iterations needed to The age of the universe ($\tau_{\text{universe}} \simeq 13.8$ Gyr) was not explicitly used as a cutoff in the MESA evolution, however an age prior is still enforced through our adopted lower bound in stellar mass of $M \geq 0.75 M_{\odot}$. Many models with $M \lesssim 0.77 M_{\odot}$ have $\tau > \tau_{\text{universe}}$ on the red giant branch for the metallicities, luminosities, and temperatures that we adopt for the modeling. Therefore, there are some model tracks calculated along the optimization where the best fit model has an age greater than τ_{universe} however, we find that the overall best fit models for both HD 128279 and HD 175305 are younger than τ_{universe}.

4. RESULTS

The best fit model parameters generated by our optimization procedure are reported in Table 4. The errors of each model parameter are determined by taking the likelihood weighted standard deviation of each parameter. This involves first taking the best fit model from each cost function iteration track (840 in total) and multiplying the model parameter value (P) by the model weight (W_{model}), given by the likelihood divided by the sampling density function from the optimization track,

$$W_{\text{model}} = \frac{L_{\text{total}}}{\sum L_{\text{total}}}, \text{ with } L_{\text{total}} = \exp(-\frac{1}{2}\chi^2_{\text{total}})/p(P). \quad (1)$$

where χ^2_{total} is defined in Appendix A and $p(P)$ is the Kernel Density Estimation based estimate of the local sampling density at that particular parameter value.

The likelihood weighted parameter values ($P \times W_{\text{model}}$) are then summed to obtain the likelihood weighted mean parameter value ($\bar{P}_{\text{Likelihood Weighted}}$) and the likelihood weighted standard deviation of each parameter is calculated as

$$\sigma_{\text{parameter}} = \sqrt{\sum W_{\text{model}} * (P - \bar{P}_{\text{Likelihood Weighted}})^2}. \quad (2)$$

To visualize the fit between the observations from M. N. Ishigaki et al. (2012) and the best-fit model spectroscopic parameters, the evolutionary track for the best fit models for HD 175305 and HD 128279 are shown in the left panels of Figure 5 and Figure 6 respectively. The background tracks in both HR-diagram panels show all the evolutionary tracks calculated over the course of the optimization process detailed in section 3. As apparent in the left-hand panels of Figure 5 and Figure 6, the best fit models' effective temperatures and luminosities agree within 1σ with the observations. We note that for both HD 175305 and HD 128279, the best fit models'

Table 4. Asteroseismic optimization modeling results for HD 128279 and HD 175305. The parameter values represent the best-fit model's mass, age, radius, initial helium abundance, mixing length, effective temperature, luminosity, and iron abundance. The parameter errors are determined by finding the likelihood weighted standard deviation of each parameter.

Target	Mass [$M_\odot$]	Age [Gyr]	Radius [$R_\odot$]	Y_0	α_{mlt}	T_{eff} [K]	Luminosity [$L_\odot$]	[Fe/H]
HD 175305	0.80 ± 0.02	11.2 ± 1.6	7.32 ± 0.07	0.26 ± 0.01	1.81 ± 0.11	5137 ± 85	33.64 ± 2.45	-1.44 ± 0.14
HD 128279	0.78 ± 0.02	12.4 ± 0.8	3.80 ± 0.03	0.25 ± 0.01	1.90 ± 0.04	5443 ± 13	11.45 ± 0.24	-2.32 ± 0.1

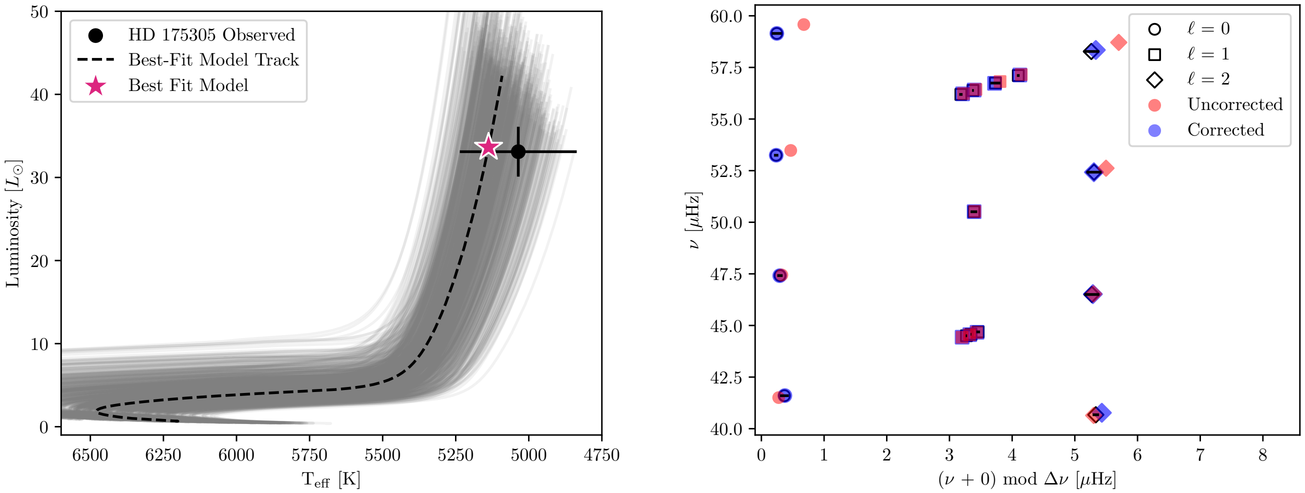

Figure 5. HD 175305 best fit model evolutionary track shown on a HR diagram (dashed line, left panel). The background evolutionary tracks on the HR diagram show the other evolutionary track calculated during the optimization process while the point with error bars display the HD 175305 observations from M. N. Ishigaki et al. (2012). The right panel frequency échelle diagram shows the best fit surface-corrected model oscillation modes in blue, matching the observed modes shown as open symbols. The red points show the best-fit model's non-surface-corrected modes.

are slightly hotter, more luminous, and more metal poor compared with the observations from M. N. Ishigaki et al. (2012). The best fit model [Fe/H] for HD 175305 ($[\mathrm{Fe/H}]_{\text{best fit}}$ = -1.44) is lower than the observed value ($[\mathrm{Fe/H}]_{\text{observed}}$ = -1.35) though the best fit model [Fe/H] value is within 1σ of the observed value from M. N. Ishigaki et al. (2012). The best fit model [Fe/H] for HD 128279 ($[\mathrm{Fe/H}]_{\text{best fit}}$ = -2.32) is also lower than the observed value ($[\mathrm{Fe/H}]_{\text{observed}}$ = -2.17), by slightly more than 1σ.

The right panels of Figure 5 and Figure 6 show the best fit models' oscillation mode frequencies (filled symbols) compared with the observed mode frequencies (open symbols) determined in this work and listed in Table 2 and Table 3 for HD 175305 and HD 128279 respectively. The red symbols show the uncorrected model mode frequencies directly from the stellar oscillation code GYRE (R. H. D. Townsend & S. A. Teitler 2013), while the blue symbols show the surface-term-corrected frequencies, which are compared with the observed mode frequencies using the two term correction from W. H. Ball & L. Gizon (2014) (see Appendix A).

5. DISCUSSION

5.1. *The Star Formation History of the Helmi Streams*

The asteroseismic best-fit age for HD 175305 is 11.2 ± 1.3 Gyr while the asteroseimic best-fit age for HD 128279 is about 1 Gyr older, at 12.4 ± 0.8 Gyr. The difference in ages is reflected in differences in chemical abundances. The older star, HD 128279, is more metal poor ([Fe/H] = -2.32) and more alpha enhanced ([α/Fe] = 0.3) compared with the younger star, HD 175305, with [Fe/H] = -1.44 and [α/Fe] = 0.23. This is broadly consistent with known chemical enrichment trends for galaxies and the Milky Way's stellar halo, which state that older populations of stars are more metal poor and alpha enhanced. Older stars are born from material mainly enhanced from core-collapse Type II supernovae, which enrich the interstellar medium with α-elements in higher concentrations compared with later-occurring Type Ia supernovae (B. M. Tinsley 1979; I. U. Roederer et al. 2010). The Helmi streams stars are known to have a large spread in metallicities, which indicates an extended star formation history by the progenitor (H. H. Koppelman et al. 2019; R. P. Naidu et al. 2020; T. Ruiz-Lara et al. 2022b).

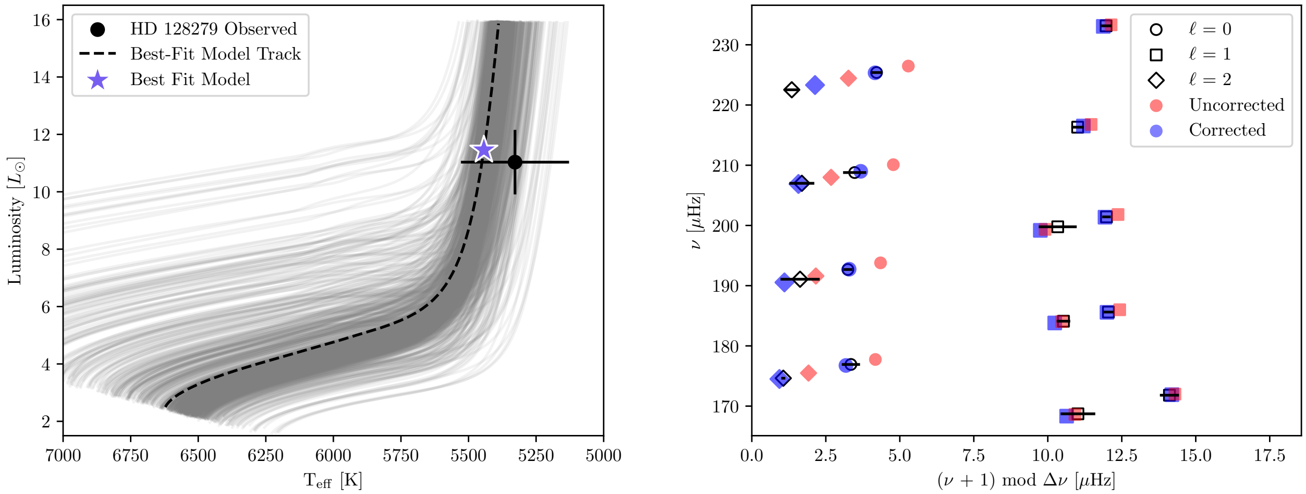

Figure 6. Same as Figure 5 but showing the best fit model for HD 128279.

The best-fit model ages we determine for these Helmi streams members using detailed asteroseismology are consistent with the formation scenario where the progenitor of the Helmi streams was a dwarf galaxy which formed a significant portion of its stars approximately 11-13 billion years ago. In particular, H. H. Koppelman et al. (2019) showed through fitting isochrones to the population of Helmi streams stars that there is a broad spread in metallicity ($-2.3 \leq$ [Fe/H] ≤ -1.0) and age (11 Gyr $\leq$ age $\leq$ 13 Gyr), consistent with the metallicity and age difference we find between HD 175305 and HD 128279. The agreement between the results of H. H. Koppelman et al. (2019), which compared spectroscopic observations to isochrones calculated using the PARSEC stellar evolution code (A. Bressan et al. 2012), and our asteroseismic results, which were determined using MESA (B. Paxton et al. 2011), shows that broadly, the ages determined for stars in the Helmi streams are generally consistant between these different methods of analysis.

Additionally, based on the color-magnitude diagram (CMD) fitting carried out in T. Ruiz-Lara et al. (2022a), the asteroseismic ages of HD 175305 and HD 128279 match a burst of star formation in the star formation history of the progenitor of the Helmi streams (the CMD fitting methodology is described in C. Gallart et al. 2024). Figure 7 shows that the best fit ages we derive for HD 175305 and HD 128279 (vertical lines in the top panel of Figure 7) match a period of high star formation rate calculated based on the most stringent membership cuts from T. Ruiz-Lara et al. (2022a). The black curve shows the star formation history of the HelmiC subset of stars from T. Ruiz-Lara et al. (2022a) while the red curve shows the star formation history of the HelmiA* subset. The HelmiA* cut is the most selective, determined by assigning line-of-sight velocities to each star in the broader HelmiA subset from T. Ruiz-Lara et al. (2022a) based on the closest star in phase space from the Gaia 6D halo sample. Then only stars with integrals of motion (L_z, $L_\perp$, and Energy) consistant with belonging to the Helmi streams (following S. S. Lövdal et al. (2022) and E. Dodd et al. (2023)) are kept in the Helmi A* subset, ensuring 100% purity. The bottom panel of Figure 7 shows the cumulative metallicity distribution of the same samples of stars from T. Ruiz-Lara et al. (2022a). We find that the best fit [Fe/H] values we determine for HD 175305 and HD 128279 are also consistent with the cumulative metallicity distribution derived in T. Ruiz-Lara et al. (2022a) (see the bottom panel of Figure 7).

Figure 8 shows the normalized star formation rate in the age-[Fe/H] plane based on the HelmiA* membership cut from T. Ruiz-Lara et al. (2022a). The normalized star formation rate is shown using a log scale along with the asteroseismic best fit stellar ages and [Fe/H], marked with stars. Figure 8 demonstrates that detailed asteroseismic modeling produces stellar ages consistent with the CMD-derived Helmi streams star formation history. HD 175305 lies directly within the region of strongest star formation [Fe/H] = -1.44 and age = 11.2 Gyr. HD 128279 is older and more metal poor ([Fe/H] = -2.32 and age = 12.4 Gyr) and therefore lies in the old, low metallicity tail of star formation in the age-[Fe/H] plane.

5.2. *Prospects for Characterizing the Helmi Streams' Progenitor*

With precise asteroseismic ages for more stream members in future work, we may begin to interpret the evolution of chemical trends across stream members. Previous spectroscopic studies of Helmi streams stars have pointed out that the stream members show a wide range in metallicity but lower α-enhancement, as well as a tighter star-to-star range in α-enhancement compared with the rest of the Milky Way halo (I. U. Roederer et al. 2010; M. Gull et al. 2021; T. Mat-

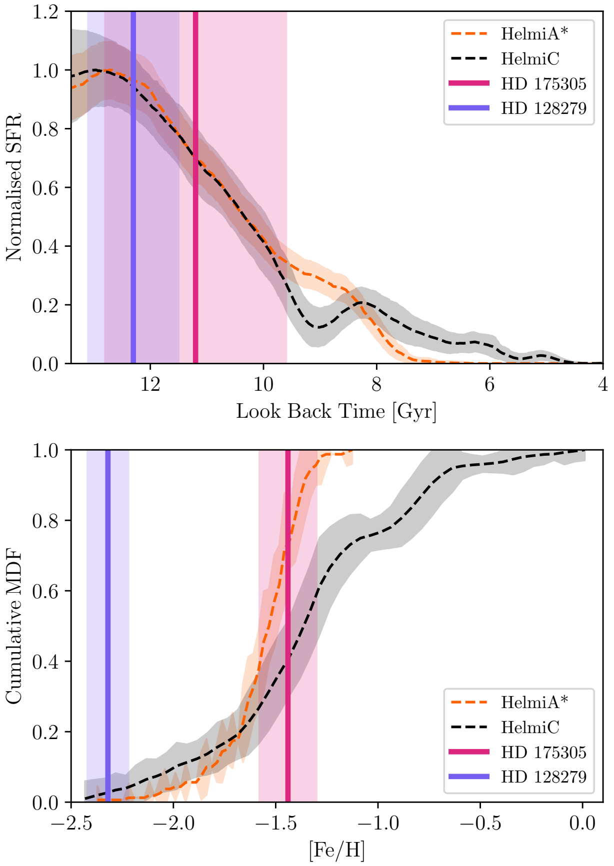

Figure 7. The top panel shows the normalized star formation rate versus look back time results from T. Ruiz-Lara et al. (2022a) for their 100% purity HelmiA* subsample (red curve) and 14% purity HelmiC subsample (black curve). The bottom panel shows the cumulative metallicity distribution function of the same Helmi streams subsamples. The thick dark red and purple vertical lines show the best fit HD 175305 and HD 128279 asteroseismic ages and [Fe/H] values in the top and bottom panels respectively, while the faint lines show the associated errors (see Table 4).

suno et al. 2022; D. Horta et al. 2023). These trends are indicative of complex star formation histories in the progenitor dwarf galaxy (T. Matsuno et al. 2022). In particular, D. Horta et al. (2023) found evidence that the [Mg/Fe] versus [Fe/H] gradient experiences a transition at a pivotal value of [Fe/H] $\sim$ 1.5 dex at which the slope becomes shallower at higher metallicities. HD 175305 and HD 128279 both populate regions close to this transition. Though we only have two stars with ages determined, the asteroseismology of more stream stars will allow us to piece together the unique chemical history of the Helmi stream more coherently.

There are multiple potential explanations for the different [α/Fe] trends between Helmi streams stars and halo stars, including potential early events in the Helmi streams progenitor which enriched it with rapid neutron-capture process (r-process) elements (M. Gull et al. 2021) and the idea that the

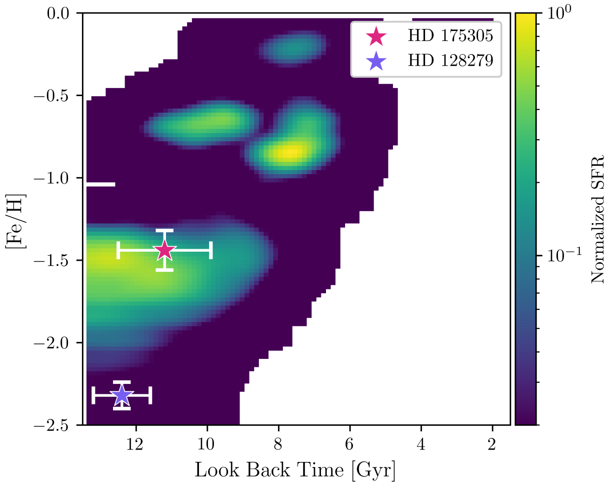

Figure 8. Normalized star formation rate in the age-[Fe/H] plane taken from the color magnitude diagram analysis of the HelmiA* sample in T. Ruiz-Lara et al. (2022a) plotted on a log scale. The star symbols show the detailed asteroseismic modeling best fit age and [Fe/H] results for HD 175305 and HD 128279.

low value of [α/Fe] is due to low star-formation efficiency at early times with bursts of star formation happening later (T. Matsuno et al. 2022). D. Horta et al. (2023) found that the evolution of the magnesium (an α-element) abundance as a function of [Fe/H] also indicates a burst of star formation, as their best fit for their sample of Helmi streams stars indicate an ‘inverted knee’, where the slope of the magnesium to iron abundance relationship becomes less negative at higher metallicities. Our results for HD 175305 and HD 128279 show that the older and lower metallicity star (HD 128279) is more enriched in α-elements including magnesium (M. N. Ishigaki et al. 2012). With the new precise asteroseismic ages, it is possible to begin to measure the [α/Fe] evolution over the history of the Helmi streams progenitor, both in [Fe/H] and time. Though with only two stars with detailed asteroseismic ages, any detailed [α/Fe]-age relationship results are still uncertain.

The Helmi streams have been long studied for the presence of heavy element enrichment within its members (e.g., I. U. Roederer et al. 2010; G. Limberg et al. 2021). These are typically r-process elements like Europium, whose enrichment within stream members provide important clues to the presence of cataclysmic events like neutron star mergers or faster-acting magnetorotational supernovae within the progenitor dwarf galaxy. Determining the enrichment pathway between these two scenarios is necessary for reconstructing the star formation history of small galaxies, understanding their chemical evolution, determining neutron star merger delay times, and studying heavy element production on a wider scale.

From the measurements of europium and barium from I. U. Roederer et al. (2010), HD 175305 is r-process enhanced (r-I, A. Frebel (2018)) while HD 128279 is not r-process enhanced. This could indicate that some r-process enhancement mechanisms in the progenitor of the Helmi streams turned on between the birth of HD 128279 and HD 175305, although the two stars may have been born in different parts of the dwarf galaxy with different r-process enrichment levels. The abundances of r-process elements such as Thorium are used to determine cosmo-chronometric ages of r-process enhanced stars (H. R. Butcher 1987; R. Cayrel et al. 2001; A. Frebel & K.-L. Kratz 2009) but when applying these techniques to HD 175305, M. Gull et al. (2021) derived an age of 0.5 Gyr, much younger than expected for a low mass giant star in a stellar stream. The determination of precise asteroseismic ages for r-process enhanced stars like HD 17530 provides a novel opportunity to calibrate cosmo-chronometric ages.

5.3. *Implications for the Use of Global Asteroseismology*

Although the masses and radii of tens of thousands of giant stars have been determined using the asteroseismic scaling relations for $\nu_{\rm max}$ ($\nu_{\rm max} \propto g\mathrm{T}_{\rm eff}^{-1/2}$, H. Kjeldsen & T. R. Bedding 1995) and $\Delta\nu$ ($\Delta\nu \propto \sqrt{\rho}$, T. M. Brown et al. 1991). T. Li et al. (2022) found systematic offsets between the inferred masses and radii determined using the global asteroseismic parameters and the model solutions established using radial ($\ell = 0$) mode asteroseismology. Currently, only a few stars in the low-metallicity regime have been studied in detail using non-radial mode frequencies (W. J. Chaplin et al. 2020; D. Huber et al. 2024). Using these scaling relations assumes that the structures of giant stars are homologous with respect to the Sun, which is not strictly true, especially as the scaling relations do not account for metallicity variances and evolutionary state. Additional verification is needed to assess the accuracy and reliability of scaling-relation derived masses and radii for low-metallicity evolved stars.

Table 5. Detailed asteroseismic modeling results for HD 128279 and HD 175305 compared with the results from Asfgrid/`modelflows` (M. Hon et al. 2024), which use global asteroseismic parameters.

	HD 175305		**HD 128279**	
	Detailed	Global	Detailed	Global
Mass ($M_\odot$)	0.80 ± 0.02	$0.92^{+0.03}_{-0.03}$	0.78 ± 0.02	$1.06^{+0.08}_{-0.05}$
Radius ($R_\odot$)	7.32 ± 0.06	$7.69^{+0.06}_{-0.06}$	3.80 ± 0.03	$4.27^{+0.09}_{-0.11}$
Age (Gyr)	11.2 ± 1.3	$8.73^{+1.32}_{-1.07}$	12.4 ± 0.8	$4.42^{+1.22}_{-0.67}$

In order to study how our detailed asteroseismic modeling results for HD 175305 and HD 128279 compare with global asteroseismic, we use Asfgrid (S. Sharma et al. 2016; D. Stello & S. Sharma 2022) to find masses and radii for our target stars based on the observed spectroscopic and global asteroseismic parameters. For each star, their observed T$_{\rm eff}$, [Fe/H], $\nu_{\rm max}$, and $\Delta\nu$ (see Table 1) are used as inputs to `modelflows` (M. Hon et al. 2024), which interpolates the Asfgrid grid of models by emulation using a neural network. The mass, radius, and age Asfgrid results for HD 175305 and HD 128279 are shown with corner plots in Figure 9 and Figure 10 and listed along with the best-fit results in Table 5. The grid-based parameter errors in Table 5 are the 16th, 50th, and 84th mass, radius, and age percentiles from the Asfgrid samples shown in figures Figure 9 and Figure 10. The best fit results from our detailed modeling are shown with black points and lines in each panel of Figure 9 and Figure 10. We note that the TACO-derived $\Delta\nu$ values for HD 175305 and HD 128279 were multiplied by 1.0109 before inputting them into `modelflows` to account for the difference between the observed $\Delta\nu$ and the frequency separation determined from non-surface-term-corrected models (L. S. Viani et al. 2018). Since the stellar modeling codes used in this work and in L. S. Viani et al. (2018) are not the same, we also tested the uncorrected $\Delta\nu$ value to confirm our results remain consistant with and without the $\Delta\nu$ correction.

Even though Asfgrid applies correction factors to the $\Delta\nu$ scaling relation, we find that the asteroseismic masses determined using the scaling relations are significantly higher than the best-fit masses we found using individual $\ell = 0, 1$, and 2 mode frequencies (Table 5). This trend agrees with previous work which found that stellar masses determined using the scaling relations were overestimated for metal-poor red giants (e.g. C. R. Epstein et al. 2014). The agreement between the global asteroseismic mass and the mass obtained using individual mode frequencies is worse for HD 127289, which may indicate the mass discrepancy expands with lower metallicity and higher α-enhancement.

Mirroring the results for global asteroseismic stellar mass determinations, the lower right histogram panels of Figure 9 and Figure 10 show that the global asteroseismic stellar age results determined using Asfgrid are underestimated compared with the results from detailed asteroseismic modeling using individual mode frequencies. The best-fit model age for HD 175305 is about 2σ larger compared with the age from global asteroseismology, while the best-fit model age for HD 128279 is much older (almost 10σ) compared with the age from global asteroseismology, which is approximately equal to the solar age. The discrepancies between the masses and ages determined for HD 128279 are much larger compared with the discrepancies between the masses and ages determined for HD 175305, potentially indicating that lower metallicity, more α-element enhanced stars like HD 128279 suffer more from errors involved with leveraging

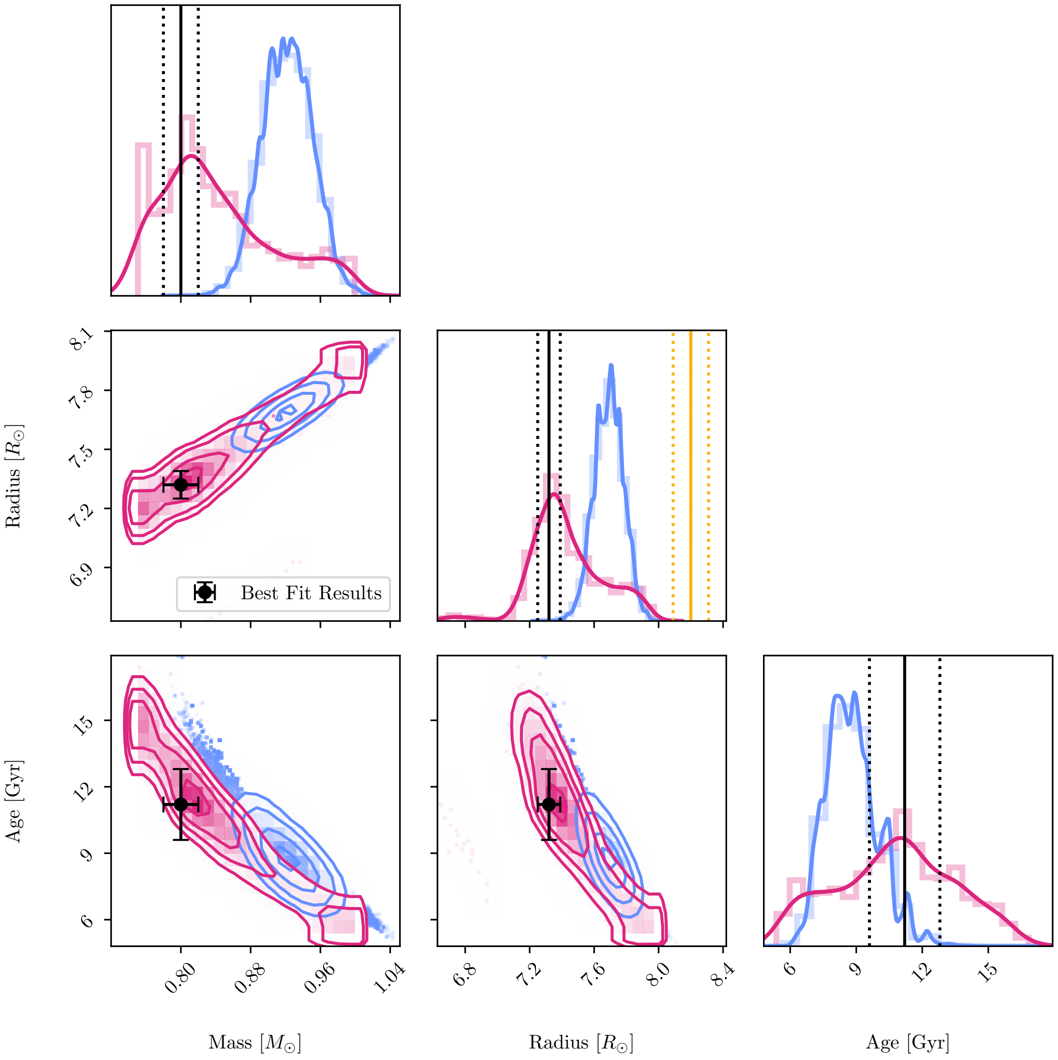

Figure 9. Asfgrid global asteroseismic results for the stellar mass, radius, and age of HD 175305 compared with the detailed asteroseismic optimization results. The blue points, histograms, and contours show the distribution of Asfgrid samples while the dark red points, histograms, and contours show the distribution of masses, radii, and ages for the best-fit model from each of the evolutionary tracks calculated as part of the optimization procedure. The black points and vertical lines in each plot show the results from the asteroseismic optimization procedure (Table 4). The vertical gold lines in the radius histogram show the interferometric radius for HD 175305 ($R = 8.2 \pm 0.11 R_\odot$) reported in I. Karovicova et al. (2020).

the global asteroseismic scaling relations, however detailed asteroseismic analyses of more stars with varying metallicities and α-abundances is needed to determine the scope and origin of the problem.

J. Schonhut-Stasik et al. (2024) present a catalog combining APOGEE spectra data and K2 asteroseismic data for 7500 evolved stars, including a large population of low-metallicity stars. As we find in this work, J. Schonhut-Stasik et al. (2024) found that the asteroseismic masses determined for low metallicity stars using global asteroseismology were significantly larger than astrophysical estimates. J. Schonhut-Stasik et al. (2024) argued this effect may be due to offsets in the adopted fundamental temperature scale for metal poor stars (J. I. González Hernández & P. Bonifacio 2009) rather than metallicity-dependent issues with the asteroseismic scaling relations However, we note that we did not use the APOGEE effective temperatures in our detailed or global asteroseismic modeling, but still find the the masses determined using global asteroseismology are much larger than masses determined using detailed asteroseismology.

The high mass, young age global asteroseismic results are also discrepant with color-magnitude diagram analysis. We compare the detailed and global asteroseismic results to the color-magnitude diagram fitting analysis of T. Ruiz-Lara et al. (2022a) in Figure 11. The younger grid based ages shown with squares in Figure 11 are less accordant with the

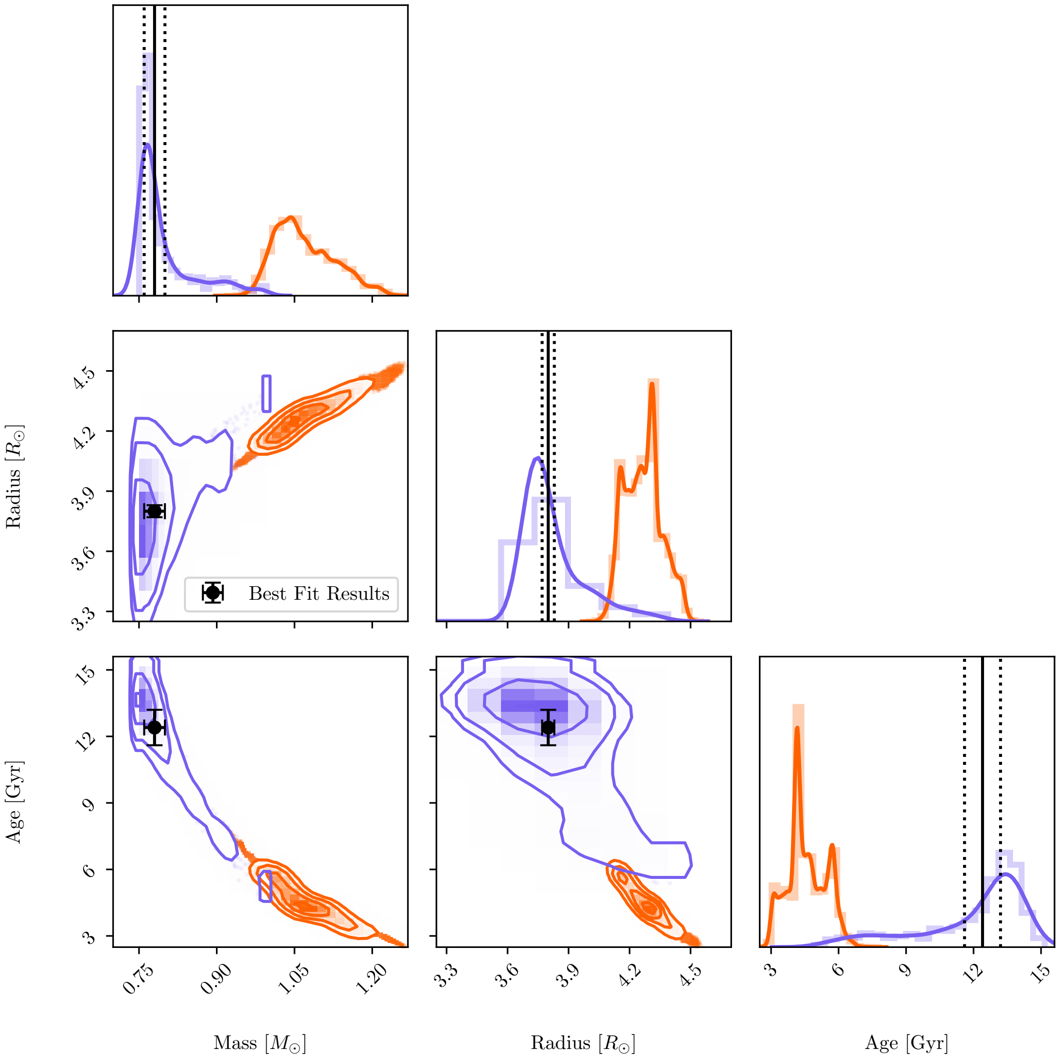

Figure 10. Asfgrid global asteroseismic results for the stellar mass, radius, and age of HD 128279 compared with the detailed asteroseismic optimization results. The orange points, histograms, and contours show the distribution of Asfgrid samples while the purple points, histograms, and contours show the distribution of masses, radii, and ages for the best-fit model from each of the evolutionary tracks calculated as part of the optimization procedure. The black points and vertical lines in each plot show the results from the asteroseismic optimization procedure (Table 4).

areas of high star formation. Additionally, the old ages we derive using detailed asteroseismology for the Helmi streams members are consistent with the idea that star formation was quenched once the progenitor dwarf galaxy merged with the Milky Way approximately 5-8 Gyr ago (H. Koppelman et al. 2018; T. Ruiz-Lara et al. 2022a; R. P. Naidu et al. 2022) while the young age grid based modeling without using individual mode frequencies produces for HD 128279 is inconsistent with this quenching theory.

We also find that the radii determined using global asteroseismic analysis are significantly larger than the radii of the best fit models we determined for HD 175305 and HD 128279. Using the SEDEX pipeline (J. Yu et al. 2023), we found that spectral energy distribution based radii results for both HD 175305 ($R_{\rm SED} = 7.6 \pm 0.7 R_\odot$) and HD 128279 ($R_{\rm SED} = 3.9 \pm 0.4 R_\odot$) are consistent to 1σ with both the detailed and global asteroseismic radii listed in Table 5.

CHARA array interferometry of HD 175305 (I. Karovicova et al. 2020) measured the star's radius to be $8.2 \pm 0.11 R_\odot$, many σ larger than the radii determined using either detailed or global asteroseismology (Figure 9). The interferometric radius of HD 175305 is also larger than the radius determined using SED fitting. Previous studies have found that stellar radii calculated using the global asteroseismic scaling relations agree with radii determined using interferometry to within ~ 5% (e.g. D. Huber et al. 2012) though seismic radii being systematically smaller than the photospheric radius is a known problem for the Sun (M. Takata & D. O. Gough

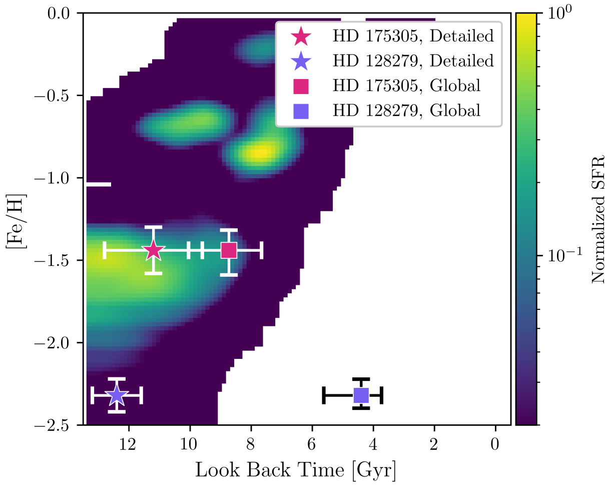

Figure 11. Normalized star formation rate in the age-[Fe/H] plane taken from the color magnitude diagram analysis of the HelmiA* sample in T. Ruiz-Lara et al. (2022a) plotted on a log scale. The symbols now show show that the detailed asteroseismic best fit optimization results for HD 175305 and HD 128279 (star symbols) agree better with the results from T. Ruiz-Lara et al. (2022a) compared with the grid based results (shown with square symbols) computed using only the global asteroseismic parameters (see Table 5).

2024). Recent detailed modeling work also found that asteroseismic radius of HD 219134 is significantly smaller than the interferometric radius (Y. Li et al. 2025). Our findings are similar to those of Y. Li et al. (2025) as we determine a best-fit model whose oscillation modes match the observed modes but whose radius is significantly smaller than radii determined using interferometry. A. L. Ash et al. (2025) found that different methods of determining correction factors used in the $\Delta\nu$ scaling relation cause differences in the asteroseismic scaling relation derived radii for luminous red giants. Thus, different implementations of a $\Delta\nu$ scaling relation correction may explain the discrepancy between the scaling relation derived radius for HD 175305 and the interferometric radius. However, the discrepancy between the best-fit model radius and the interferometric radius is likely due to the fact that matching surface corrected model mode frequencies to observed oscillations does well at modeling the deep internal structure but not the near-surface layers. Improved agreement between asteroseismic model radii and interferometric radii will rely on better models for the atmosphere of stars and new treatments for correcting stellar model oscillation frequencies for near-surface effects. We also note that the effective temperature of HD 175305 determined using interferometry ($T_{\rm eff} = 4850 \pm 118$ K I. Karovicova et al. 2020) was significantly lower than the temperature we employed in our modeling. In this work we used the effective temperature from M. N. Ishigaki et al. (2012) in order to stay consistant between our modelling for both HD 175305, where interferometric data is avaliable, and HD 128279, where interferometric data is not avaliable.

5.4. *Potential Constraints from Gravity Mode Period Spacings*

Thus far, we have assumed that HD 175305 and HD 128279 are stars on their first ascent up the red giant branch, such that they are burning hydrogen in a shell around an inert helium core. This assumption is made based on the two stars' kinematic membership in the relatively old Helmi streams structure and its low metallicity. In this section, we examine the assumption that HD 175305 and HD 128279 are first ascent red giant branch stars by examining the stars' gravity mode (g-mode) period spacing ($\Delta\Pi_\ell$). This quantity refers to the asymptotic period spacing between consecutive g-modes of the same spherical degree ℓ and probes the core region of giant stars as its value depends on the buoyancy frequency profile in the core,

$$\Delta\Pi_\ell = \frac{2\pi^2}{\sqrt{\ell(\ell+1}}\left(\int_{\rm core}\frac{N}{r}dr\right)^{-1} \tag{3}$$

where N is the Brunt–Väisälä, r is the radius coordinate, and ℓ is the angular degree.

Measurements of $\Delta\Pi_{\ell=1}$ are especially valuable for determining the evolutionary state and ages of red giants. Larger values of $\Delta\Pi_{\ell=1}$ indicate a less compact core and are generally representative of core-Helium burning giants, while hydrogen-shell burning giants tend to have more compact, degenerate cores the lead to smaller $\Delta\Pi_{\ell=1}$ (T. R. Bedding et al. 2011). The boundary between these two evolutionary phases is clearly defined for low-mass ($M < 1.2M_\odot$) red giant branch stars, whereby those with $\Delta\Pi_{\ell=1} < 100$ s are hydrogen-shell burning and those higher $\Delta\Pi_{\ell=1}$ are core-helium burning stars (B. Mosser et al. 2015; M. Vrard et al. 2016; J. S. Kuszlewicz et al. 2023). Beyond a determination of evolutionary phase, $\Delta\Pi_{\ell=1}$ may also provide an additional asteroseismic constraint to include in stellar modeling.

We attempted to use the peakbagging tools `PBJam/reggae` (M. B. Nielsen et al. 2021; J. Ong et al. 2024) to derive $\Delta\Pi_{\ell=1}$ from the power spectra of HD 175305, but were unable to do so with a high degree of confidence assuming HD 175305 is a first-ascent giant. This is due to the unavailability of a suitable Bayesian prior from `PBJam/reggae` due to a combination of the low-metallicity and advanced evolutionary state of HD 175305. Therefore, we cannot definatively rule out HD 175305 being a core Helium burning star based solely on the asteroseismic data. If HD 175305 was a helium burning star, it would be much younger, unless it reached its current structure through a mass transfer or merger event earlier in its evolutionary history (N. Z. Rui & J. Fuller 2021). In this scenario, HD 175305 would appear younger than its true age, even when analyzed using asteroseismic techniques. The origins of young α-rich stars have been studied in recent years through a combination of asteroseismic and spectroscopic techniques and binary interactions of older stars appear important to the existence of the seemingly young α-rich stars (C. Chiappini et al. 2015; R. P. Martin et al. 2015; P. Jofré et al. 2023; J. Yu et al. 2024), however genuinely young α-rich also appear (Y. Lu et al. 2025). Young α-rich stars are a minority, representing approximately 10% of α-enhanced field stars (V. Grisoni et al. 2024). Therefore, there is a low chance HD 175305 is truly one of these objects, though additional asteroseismic measurements of the g-mode period spacing of HD 175305 would be able to determine the evolutionary state with more certainty.

We were able to determine a g-mode period spacing of $\Delta\Pi_{\ell=1}$ for HD 128279, finding $\Delta\Pi_{\ell=1} = 83.45 \pm 0.5$ seconds using `PBJam/reggae`. This is done by first fitting a model for the $\ell = 0$ and $\ell = 2$ modes only against the power spectrum (using `PBJam` version 2.0), which was divided out to produce a residual power spectrum containing power from only dipole-mode oscillations. Figure 13 shows this residual power spectrum, in the form of a stretched period-échelle power diagram (as constructed following J. M. J. Ong & C. Gehan 2023), where the power spectrum is phase-folded by the g-mode period spacing $\Delta\Pi_1$, after applying a nonlinear coordinate transformation which undoes the coupling between the p- and g-mode cavities (e.g. B. Mosser et al. 2015). The asymptotic period spacing is determined using `reggae`, taking a maximum likelihood estimate given a prior on the gravity mode phase shift (ϵ_g) as being 0.78 (which is the value that emerges from asymptotic analysis of high-order dipole g-modes: J. Provost & G. Berthomieu 1986). Figure 12 shows that phase-folding by this value of $\Delta\Pi_{\ell=1}$ results in the g-mode peaks forming a single vertically-aligned ridge along the vertical gray dashed line in the échelle power diagram.

Given that HD 128278 has only been observed for two, non-contiguous sectors, the data is insufficient to simultaneously and independently constrain the pure p-mode frequencies (one parameter for each radial order), ϵ_g, the coupling factor (q), and $\Delta\Pi_{\ell=1}$. This results in a relatively high uncertainty for the observed $\Delta\Pi_{\ell=1}$ value (0.5 seconds) — which is orders of magnitude less precise than those measured from Kepler, or from the TESS continuous viewing zones — as $\Delta\Pi_{\ell=1}$ value is statistically degenerate with other g-mode parameters such as ϵ_g. Figure 13 shows this empirical value of $\Delta\Pi_{\ell=1}$ using the orange vertical line, compared to a histogram showing the $\Delta\Pi_{\ell=1}$ values from each of the best-fit models along each of the tracks calculated as part of the asteroseismic optimization procedure. The best fit model we constructed for HD 128279 during the optimisation procedure has an asymptotic period spacing value of $\Delta\Pi_{\ell=1} = 82.4$ s (purple vertical line in the right panel of Figure 13), which is close to the value determined directly from the HD 128279 power spectrum. Even though $\Delta\Pi_{\ell=1}$ values were not explicitly included in the asteroseismic optimization procedure, the best fit models of HD 128279 roughly agree with the observed $\Delta\Pi_{\ell=1}$ value. Including a $\Delta\Pi_{\ell=1}$ constraint does not change the asteroseismic modeling results significantly, owing to the lack of precision in this constraint. However, it confirms our identification of HD 128279 as a first-ascent red giant.

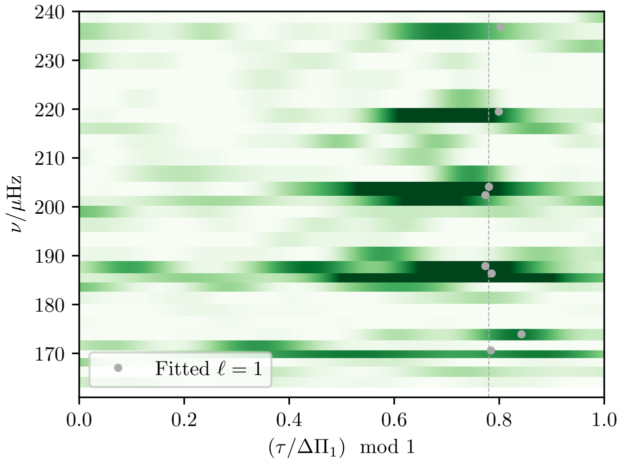

Figure 12. The `reggae`-generated stretched period échelle power diagram (frequency versus the stretched period folded by the asymptotic period spacing) for HD 128279. Before plotting, the `PBJam`-generated fit to the $\ell = 0$ and $\ell = 2$ modes divided out from the power spectra, so that only residual power from dipole modes is depicted. The gray points show the dipolar mode frequencies from Table 3 and the vertical gray dashed line shows the value of ϵ_g (0.78).

6. SUMMARY AND CONCLUSION

We have conducted a detailed asteroseismic analysis of two halo star members of the Helmi streams (A. Helmi et al. 1999), which are remnants of a system believed to have merged with the Milky Way 5 to 8 billion years ago (A. A. Kepley et al. 2007; H. Koppelman et al. 2018; T. Ruiz-Lara et al. 2022a; H. C. Woudenberg & A. Helmi 2024). These target stars were identified in E. Dodd et al. (2023) by analyzing the stellar abundance data with 6D Gaia position and velocity measurements and grouping stars to determine substructures in the local stellar halo.

With data from TESS (G. R. Ricker et al. 2015) we used the peak-bagging code TACO (N. Themeßl et al. 2020) to analyze the light curves of HD 175305 and HD 128279 and determined the global asteroseismic parameters ($\nu_{\max}$ and $\Delta\nu$) as well as the radial, dipole, and quadrupole oscillation mode frequencies of the stars. The global asteroseismic parameters as well as the spectroscopic parameters for our target stars are listed in Table 1 and the mode frequencies for HD 175305 and HD 128279 are listed in Table 2 and Table 3 respectively.

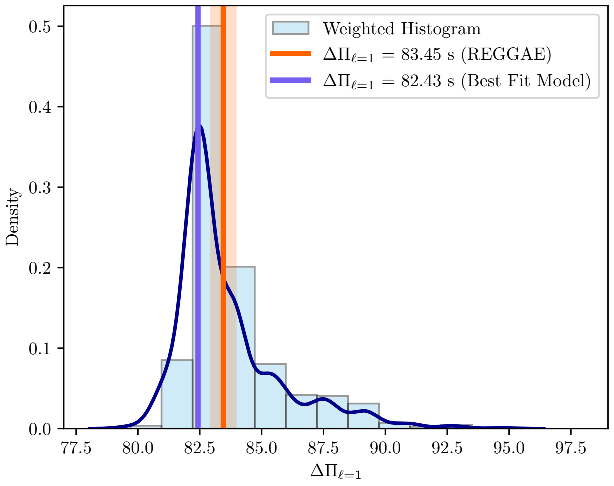

Figure 13. The likelihood weighted histogram of $\Delta\Pi_{\ell=1}$ values from each of the best-fit models from every evolutionary track calculated as part of the optimization procedure (Appendix A). The solid dark blue curve shows the kernel density estimate of the same likelihood weighted $\Delta\Pi_{\ell=1}$ values. The overall best fit model $\Delta\Pi_{\ell=1}$ value is shown with a vertical purple line and the observed $\Delta\Pi_{\ell=1}$ value obtained using `PBJam/reggae` is shown with the vertical orange line.

In order to determine the best fit parameters for these Helmi streams stars, we developed an asteroseismic modeling procedure which creates models using the stellar evolutionary code MESA, calculates the model oscillation frequencies using GYRE, and compares the spectroscopic and asteroseismic quantities of the models along an evolutionary track to the observed properties. The best fit model parameters for HD 175305 and HD 128279 are listed in Table 4 and visualized in Figure 5 and Figure 6, respectively.

From our detailed asteroseismic modelling results, our takeaway points are:

1. Grid based modelling using only global asteroseismic parameters is inadequate for accurately determining the stellar parameters of metal-poor stars in the Halo. Our best fit masses and radii for both HD 175305 ($M = 0.80 M_\odot$, $R = 7.32 R_\odot$) and HD 128279 ($M = 0.78 M_\odot$, $R = 3.8 R_\odot$) are lower than the masses and radii determine using the global asteroseismic parameters (Table 5). Additionally, the asteroseismic ages we determine for HD 175305 and HD 128279 are older compared with ages determined without individual mode frequencies, showing that detailed asteroseismology with individual modes is necessary to study metal-poor halo stars such as those associated with the Helmi streams, in agreement with previous asteroseismic studies (C. R. Epstein et al. 2014; D. Huber et al. 2024).
2. The best fit asteroseismic ages and other parameters we determine for HD 175305 (11.2 Gyr) and HD 128279 (12.4 Gyr) are consistent with previous studies of the star formation histories of the Helmi streams (H. H. Koppelman et al. 2019; R. P. Naidu et al. 2022; T. Ruiz-Lara et al. 2022a).
3. The old age of HD 128279 (12.4 Gyr) places a lower bound on when stars began to form in the progenitor of the Helmi streams.
4. Precise asteroseismic ages for stars in Halo substructures may be combined with chemical abundance measurements to precisely time when *r*-process enrichment occurred in accreted dwarf galaxies.

As we have shown, asteroseismology enables the precise dating of individual red giants in different components of the Milky Way's halo. As TESS continues to measure the flux of more halo stars and survey efforts produce precise chemical abundances for larger numbers of stars, additional detailed asteroseismic analyses of more halo stars will become possible, allowing for precise studies of the ages and stellar properties for many stars in different kinematic components of our galaxy. Future asteroseismic studies will produce precise ages for more stars in Milky Way substructures, especially with the advent of the Roman space telescope (D. Huber et al. 2023) and the PLAnetary Transits and Oscillations of stars mission (PLATO H. Rauer et al. 2022). Many precise ages of halo stars will therefore soon be available to calibrate the cosmochronometry of stellar streams and date the processes which enrich galaxies with heavy elements.

ACKNOWLEDGEMENTS

CJL acknowledges support from a Gruber Science Fellowship and NSF grant AST-2205026. M.H. acknowledges support from NASA grant 80NSSC24K0228. JMJO acknowledges support from NASA through the NASA Hubble Fellowship grant HST-HF2-51517.001, awarded by the Space Telescope Science Institute (STScI). RAG and DBP acknowledge the support from the GOLF and PLATO Centre National D'Études Spatiales grants. TRL acknowledges support from Juan de la Cierva fellowship (IJC2020-043742-I) and Ramón y Cajal fellowship (RYC2023-043063-I, financed by MCIU/AEI/10.13039/501100011033 and by the FSE+). AH is grateful for financial support through a Spinoza Grant from the Dutch Research Council (NWO). We also thank Yaguang Li, Dan Huber, Sarbani Basu, Yasmeen Asali, William Cerny, as well as Earl Bellinger and the Yale AstroML group for their useful and constructive discussion. We acknowledge the use of TESS High-Level Science Products (HLSP) produced by the Quick-Look Pipeline

(QLP) at the TESS Science Office at MIT, which are publicly available from the Mikulski Archive for Space Telescopes (MAST) at STScI. The specific observations analyzed can be accessed via https://doi.org/10.17909/qps3-3v44. Funding for the TESS mission is provided by the NASA Explorer Program. STScI is operated by the Association of Universities for Research in Astronomy, Inc., under NASA contract NAS 5–26555.

Software: MESA (B. Paxton et al. 2011, 2013, 2015, 2018, 2019; A. S. Jermyn et al. 2023), GYRE (R. H. D. Townsend & S. A. Teitler 2013) , SciPy (P. Virtanen et al. 2020), Pandas (J. Reback et al. 2021), Astropy (Astropy Collaboration et al. 2013, 2018, 2022), Lightkurve (Lightkurve Collaboration et al. 2018), `PBJam` (M. B. Nielsen et al. 2021), `reggae` (J. Ong et al. 2024), TACO (N. Themeßl et al. 2020), YABOX (P. R. Mier 2017), Asfgrid (S. Sharma et al. 2016; D. Stello & S. Sharma 2022)

The MESA and GYRE inlists we used to generate our models and calculate model frequencies are archived on Zenodo and can be downloaded at zenodo.org/records/15102877. We also include the MESA evolutionary tracks and profiles for our best-fit models.

REFERENCES

Abdurro'uf, Accetta, K., Aerts, C., et al. 2022, ApJS, 259, 35, doi: 10.3847/1538-4365/ac4414

Alongi, M., Bertelli, G., Bressan, A., & Chiosi, C. 1991, A&A, 244, 95

Ash, A. L., Pinsonneault, M. H., Vrard, M., & Zinn, J. C. 2025, ApJ, 979, 135, doi: 10.3847/1538-4357/ad9b18

Astropy Collaboration, Robitaille, T. P., Tollerud, E. J., et al. 2013, A&A, 558, A33, doi: 10.1051/0004-6361/201322068

Astropy Collaboration, Price-Whelan, A. M., Sipőcz, B. M., et al. 2018, AJ, 156, 123, doi: 10.3847/1538-3881/aabc4f

Astropy Collaboration, Price-Whelan, A. M., Lim, P. L., et al. 2022, ApJ, 935, 167, doi: 10.3847/1538-4357/ac7c74

Ball, W. H., & Gizon, L. 2014, A&A, 568, A123, doi: 10.1051/0004-6361/201424325

Basu, S., & Chaplin, W. J. 2017, Asteroseismic Data Analysis: Foundations and Techniques

Basu, S., & Kinnane, A. 2018, ApJ, 869, 8, doi: 10.3847/1538-4357/aae922

Bedding, T. R., Mosser, B., Huber, D., et al. 2011, Nature, 471, 608, doi: 10.1038/nature09935

Beers, T. C., Chiba, M., Yoshii, Y., et al. 2000, AJ, 119, 2866, doi: 10.1086/301410

Bland-Hawthorn, J., & Maloney, P. R. 2002, in Astronomical Society of the Pacific Conference Series, Vol. 254, Extragalactic Gas at Low Redshift, ed. J. S. Mulchaey & J. T. Stocke, 267, doi: 10.48550/arXiv.astro-ph/0110044

Bonaca, A., & Price-Whelan, A. M. 2025, NewAR, 100, 101713, doi: 10.1016/j.newar.2024.101713

Borre, C. C., Aguirre Børsen-Koch, V., Helmi, A., et al. 2022, MNRAS, 514, 2527, doi: 10.1093/mnras/stac1498

Bressan, A., Marigo, P., Girardi, L., et al. 2012, MNRAS, 427, 127, doi: 10.1111/j.1365-2966.2012.21948.x

Broersen, P. 2009, IEEE Transactions on Instrumentation Measurement, 58, 1380, doi: 10.1109/TIM.2008.2009201

Brown, T. M., Gilliland, R. L., Noyes, R. W., & Ramsey, L. W. 1991, ApJ, 368, 599, doi: 10.1086/169725

Butcher, H. R. 1987, Nature, 328, 127, doi: 10.1038/328127a0

Cayrel, R., Hill, V., Beers, T. C., et al. 2001, Nature, 409, 691, doi: 10.1038/35055507

Chaplin, W. J., Serenelli, A. M., Miglio, A., et al. 2020, Nature Astronomy, 4, 382, doi: 10.1038/s41550-019-0975-9

Chiappini, C., Anders, F., Rodrigues, T. S., et al. 2015, A&A, 576, L12, doi: 10.1051/0004-6361/201525865

Chiba, M., & Beers, T. C. 2000, AJ, 119, 2843, doi: 10.1086/301409

Cox, J. P., & Giuli, R. T. 1968, Principles of stellar structure (Cambridge Scientific Publishers)

Cunha, M. S., Roxburgh, I. W., Aguirre Børsen-Koch, V., et al. 2021, MNRAS, 508, 5864, doi: 10.1093/mnras/stab2886

Das, P., Hawkins, K., & Jofré, P. 2020, MNRAS, 493, 5195, doi: 10.1093/mnras/stz3537

Davies, G. R., Handberg, R., Miglio, A., et al. 2014, MNRAS, 445, L94, doi: 10.1093/mnrasl/slu143

Dodd, E., Callingham, T. M., Helmi, A., et al. 2023, A&A, 670, L2, doi: 10.1051/0004-6361/202244546

Epstein, C. R., Elsworth, Y. P., Johnson, J. A., et al. 2014, ApJL, 785, L28, doi: 10.1088/2041-8205/785/2/L28

Frebel, A. 2018, Annual Review of Nuclear and Particle Science, 68, 237, doi: 10.1146/annurev-nucl-101917-021141

Frebel, A., & Kratz, K.-L. 2009, in IAU Symposium, Vol. 258, The Ages of Stars, ed. E. E. Mamajek, D. R. Soderblom, & R. F. G. Wyse, 449–456, doi: 10.1017/S1743921309032104

Gaia Collaboration, Prusti, T., de Bruijne, J. H. J., et al. 2016, A&A, 595, A1, doi: 10.1051/0004-6361/201629272

Gaia Collaboration, Brown, A. G. A., Vallenari, A., et al. 2018, A&A, 616, A1, doi: 10.1051/0004-6361/201833051

Gaia Collaboration, Brown, A. G. A., Vallenari, A., et al. 2021, A&A, 649, A1, doi: 10.1051/0004-6361/202039657

Gallart, C., Surot, F., Cassisi, S., et al. 2024, A&A, 687, A168, doi: 10.1051/0004-6361/202349078

García, R. A., Mathur, S., Pires, S., et al. 2014, A&A, 568, A10, doi: 10.1051/0004-6361/201323326

García, R. A., Palakkatharappil, D. B., Bugnet, L., et al. 2024, in 8th TESS/15th Kepler Asteroseismic Science Consortium Workshop, 123, doi: 10.5281/zenodo.13647412

González-Cuesta, L., Mathur, S., García, R. A., et al. 2023, A&A, 674, A106, doi: 10.1051/0004-6361/202244577

González Hernández, J. I., & Bonifacio, P. 2009, A&A, 497, 497, doi: 10.1051/0004-6361/200810904

Grec, G., Fossat, E., & Pomerantz, M. A. 1983, SoPh, 82, 55, doi: 10.1007/BF00145545

Grevesse, N., & Sauval, A. J. 1998, SSRv, 85, 161, doi: 10.1023/A:1005161325181

Grillmair, C. J., & Carlin, J. L. 2016, in Astrophysics and Space Science Library, Vol. 420, Tidal Streams in the Local Group and Beyond, ed. H. J. Newberg & J. L. Carlin, 87, doi: 10.1007/978-3-319-19336-6_4

Grisoni, V., Chiappini, C., Miglio, A., et al. 2024, A&A, 683, A111, doi: 10.1051/0004-6361/202347440

Gull, M., Frebel, A., Hinojosa, K., et al. 2021, ApJ, 912, 52, doi: 10.3847/1538-4357/abea1a

Helmi, A. 2020, ARA&A, 58, 205, doi: 10.1146/annurev-astro-032620-021917

Helmi, A., Babusiaux, C., Koppelman, H. H., et al. 2018, Nature, 563, 85, doi: 10.1038/s41586-018-0625-x

Helmi, A., & de Zeeuw, P. T. 2000, MNRAS, 319, 657, doi: 10.1046/j.1365-8711.2000.03895.x

Helmi, A., White, S. D. M., de Zeeuw, P. T., & Zhao, H. 1999, Nature, 402, 53, doi: 10.1038/46980

Hon, M., Kuszlewicz, J. S., Huber, D., Stello, D., & Reyes, C. 2022, AJ, 164, 135, doi: 10.3847/1538-3881/ac8931

Hon, M., Li, Y., & Ong, J. 2024, ApJ, 973, 154, doi: 10.3847/1538-4357/ad6320

Hon, M., Huber, D., Kuszlewicz, J. S., et al. 2021, ApJ, 919, 131, doi: 10.3847/1538-4357/ac14b1

Horta, D., Schiavon, R. P., Mackereth, J. T., et al. 2023, MNRAS, 520, 5671, doi: 10.1093/mnras/stac3179

Huang, C. X., Vanderburg, A., Pál, A., et al. 2020a, Research Notes of the American Astronomical Society, 4, 204, doi: 10.3847/2515-5172/abca2e

Huang, C. X., Vanderburg, A., Pál, A., et al. 2020b, Research Notes of the American Astronomical Society, 4, 206, doi: 10.3847/2515-5172/abca2d

Huber, D., Ireland, M. J., Bedding, T. R., et al. 2012, ApJ, 760, 32, doi: 10.1088/0004-637X/760/1/32

Huber, D., Pinsonneault, M., Beck, P., et al. 2023, arXiv e-prints, arXiv:2307.03237, doi: 10.48550/arXiv.2307.03237

Huber, D., Slumstrup, D., Hon, M., et al. 2024, ApJ, 975, 19, doi: 10.3847/1538-4357/ad7110

Ibata, R. A., Gilmore, G., & Irwin, M. J. 1994, Nature, 370, 194, doi: 10.1038/370194a0

Ishigaki, M. N., Chiba, M., & Aoki, W. 2012, ApJ, 753, 64, doi: 10.1088/0004-637X/753/1/64

Jenkins, J. M. 2017,, Kepler Science Document KSCI-19081-002, id. 2, Edited by Jon M. Jenkins.

Jermyn, A. S., Bauer, E. B., Schwab, J., et al. 2023, ApJS, 265, 15, doi: 10.3847/1538-4365/acae8d

Jofré, P., Jorissen, A., Aguilera-Gómez, C., et al. 2023, A&A, 671, A21, doi: 10.1051/0004-6361/202244524

Karovicova, I., White, T. R., Nordlander, T., et al. 2020, A&A, 640, A25, doi: 10.1051/0004-6361/202037590

Kepley, A. A., Morrison, H. L., Helmi, A., et al. 2007, AJ, 134, 1579, doi: 10.1086/521429

Khan, S., Hall, O. J., Miglio, A., et al. 2018, ApJ, 859, 156, doi: 10.3847/1538-4357/aabf90

Kjeldsen, H., & Bedding, T. R. 1995, A&A, 293, 87. https://arxiv.org/abs/astro-ph/9403015

Koppelman, H., Helmi, A., & Veljanoski, J. 2018, ApJL, 860, L11, doi: 10.3847/2041-8213/aac882

Koppelman, H. H., Helmi, A., Massari, D., Roelenga, S., & Bastian, U. 2019, A&A, 625, A5, doi: 10.1051/0004-6361/201834769

Kunimoto, M., Tey, E., Fong, W., et al. 2022, Research Notes of the American Astronomical Society, 6, 236, doi: 10.3847/2515-5172/aca158

Kunimoto, M., Huang, C., Tey, E., et al. 2021, Research Notes of the American Astronomical Society, 5, 234, doi: 10.3847/2515-5172/ac2ef0

Kuszlewicz, J. S., Hon, M., & Huber, D. 2023, ApJ, 954, 152, doi: 10.3847/1538-4357/ace598

Li, T., Li, Y., Bi, S., et al. 2022, ApJ, 927, 167, doi: 10.3847/1538-4357/ac4fbf

Li, Y., Bedding, T. R., Stello, D., et al. 2023, MNRAS, 523, 916, doi: 10.1093/mnras/stad1445

Li, Y., Huber, D., Ong, J. M. J., et al. 2025, arXiv e-prints, arXiv:2502.00971. https://arxiv.org/abs/2502.00971

Lightkurve Collaboration, Cardoso, J. V. d. M. a., Hedges, C., et al. 2018, http://ascl.net/1812.013

Limberg, G., Santucci, R. M., Rossi, S., et al. 2021, ApJL, 913, L28, doi: 10.3847/2041-8213/ac0056

Lindsay, C. J., Ong, J. M. J., & Basu, S. 2022, ApJ, 931, 116, doi: 10.3847/1538-4357/ac67ed

Lindsay, C. J., Ong, J. M. J., & Basu, S. 2024, ApJ, 965, 171, doi: 10.3847/1538-4357/ad2ae5

Lövdal, S. S., Ruiz-Lara, T., Koppelman, H. H., et al. 2022, A&A, 665, A57, doi: 10.1051/0004-6361/202243060

Lu, Y., Colman, I. L., Sayeed, M., et al. 2025, AJ, 169, 168, doi: 10.3847/1538-3881/ada9e0

Martin, R. P., Andrievsky, S. M., Kovtyukh, V. V., et al. 2015, MNRAS, 449, 4071, doi: 10.1093/mnras/stv590

Matsuno, T., Dodd, E., Koppelman, H. H., et al. 2022, A&A, 665, A46, doi: 10.1051/0004-6361/202243609

Mier, P. R. 2017,, v1.0.3 Zenodo, doi: 10.5281/zenodo.848679

Mosser, B., Vrard, M., Belkacem, K., Deheuvels, S., & Goupil, M. J. 2015, A&A, 584, A50, doi: 10.1051/0004-6361/201527075

Naidu, R. P., Conroy, C., Bonaca, A., et al. 2020, ApJ, 901, 48, doi: 10.3847/1538-4357/abaef4

Naidu, R. P., Conroy, C., Bonaca, A., et al. 2022, arXiv e-prints, arXiv:2204.09057, doi: 10.48550/arXiv.2204.09057

Nielsen, M. B., Davies, G. R., Ball, W. H., et al. 2021, AJ, 161, 62, doi: 10.3847/1538-3881/abcd39

Ong, J., Nielsen, M., Hatt, E., & Davies, G. 2024, The Journal of Open Source Software, 9, 6588, doi: 10.21105/joss.06588

Ong, J. M. J., & Basu, S. 2020, ApJ, 898, 127, doi: 10.3847/1538-4357/ab9ffb

Ong, J. M. J., Basu, S., & McKeever, J. M. 2021, ApJ, 906, 54, doi: 10.3847/1538-4357/abc7c1

Ong, J. M. J., & Gehan, C. 2023, ApJ, 946, 92, doi: 10.3847/1538-4357/acbf2f

Paxton, B., Bildsten, L., Dotter, A., et al. 2011, ApJS, 192, 3, doi: 10.1088/0067-0049/192/1/3

Paxton, B., Cantiello, M., Arras, P., et al. 2013, ApJS, 208, 4, doi: 10.1088/0067-0049/208/1/4

Paxton, B., Marchant, P., Schwab, J., et al. 2015, ApJS, 220, 15, doi: 10.1088/0067-0049/220/1/15

Paxton, B., Schwab, J., Bauer, E. B., et al. 2018, ApJS, 234, 34, doi: 10.3847/1538-4365/aaa5a8

Paxton, B., Smolec, R., Schwab, J., et al. 2019, ApJS, 243, 10, doi: 10.3847/1538-4365/ab2241

Price-Whelan, A. M., & Bonaca, A. 2018, ApJL, 863, L20, doi: 10.3847/2041-8213/aad7b5

Provost, J., & Berthomieu, G. 1986, A&A, 165, 218

Rauer, H., Aerts, C., Deleuil, M., et al. 2022, in European Planetary Science Congress, EPSC2022–453, doi: 10.5194/epsc2022-453

Reback, J., Mendel, J. B., McKinney, W., et al. 2021,, v1.3.0 Zenodo, doi: 10.5281/zenodo.3509134

Richter, P. 2017, in Astrophysics and Space Science Library, Vol. 430, Gas Accretion onto Galaxies, ed. A. Fox & R. Davé, 15, doi: 10.1007/978-3-319-52512-9_2

Ricker, G. R., Winn, J. N., Vanderspek, R., et al. 2015, Journal of Astronomical Telescopes, Instruments, and Systems, 1, 014003, doi: 10.1117/1.JATIS.1.1.014003

Roederer, I. U., Sneden, C., Thompson, I. B., Preston, G. W., & Shectman, S. A. 2010, ApJ, 711, 573, doi: 10.1088/0004-637X/711/2/573

Rui, N. Z., & Fuller, J. 2021, MNRAS, 508, 1618, doi: 10.1093/mnras/stab2528

Ruiz-Lara, T., Gallart, C., Bernard, E. J., & Cassisi, S. 2020, Nature Astronomy, 4, 965, doi: 10.1038/s41550-020-1097-0

Ruiz-Lara, T., Helmi, A., Gallart, C., Surot, F., & Cassisi, S. 2022a, A&A, 668, L10, doi: 10.1051/0004-6361/202244127

Ruiz-Lara, T., Matsuno, T., Lövdal, S. S., et al. 2022b, A&A, 665, A58, doi: 10.1051/0004-6361/202243061

Schonhut-Stasik, J., Zinn, J. C., Stassun, K. G., et al. 2024, AJ, 167, 50, doi: 10.3847/1538-3881/ad0b13

Searle, L., & Zinn, R. 1978, ApJ, 225, 357, doi: 10.1086/156499

Sharma, S., Stello, D., Bland-Hawthorn, J., Huber, D., & Bedding, T. R. 2016, ApJ, 822, 15, doi: 10.3847/0004-637X/822/1/15

Soubiran, C., Creevey, O. L., Lagarde, N., et al. 2024, A&A, 682, A145, doi: 10.1051/0004-6361/202347136

Springel, V., White, S. D. M., Jenkins, A., et al. 2005, Nature, 435, 629, doi: 10.1038/nature03597

Stassun, K. G., Oelkers, R. J., Paegert, M., et al. 2019, AJ, 158, 138, doi: 10.3847/1538-3881/ab3467

Stello, D., & Sharma, S. 2022, Research Notes of the American Astronomical Society, 6, 168, doi: 10.3847/2515-5172/ac8b12

Takata, M., & Gough, D. O. 2024, MNRAS, 527, 1283, doi: 10.1093/mnras/stad3206

Tassoul, M. 1980, ApJS, 43, 469, doi: 10.1086/190678

Themeßl, N., Kuszlewicz, J. S., García Saravia Ortiz de Montellano, A., & Hekker, S. 2020, in Stars and their Variability Observed from Space, ed. C. Neiner, W. W. Weiss, D. Baade, R. E. Griffin, C. C. Lovekin, & A. F. J. Moffat, 287–291

Thoul, A. A., Bahcall, J. N., & Loeb, A. 1994, ApJ, 421, 828, doi: 10.1086/173695

Tinsley, B. M. 1979, ApJ, 229, 1046, doi: 10.1086/157039

Townsend, R. H. D., & Teitler, S. A. 2013, MNRAS, 435, 3406, doi: 10.1093/mnras/stt1533

Twicken, J. D., Jenkins, J. M., Seader, S. E., et al. 2016, AJ, 152, 158, doi: 10.3847/0004-6256/152/6/158

Viani, L. S., Basu, S., Ong J., M. J., Bonaca, A., & Chaplin, W. J. 2018, ApJ, 858, 28, doi: 10.3847/1538-4357/aab7eb

Virtanen, P., Gommers, R., Oliphant, T. E., et al. 2020, Nature Methods, 17, 261, doi: 10.1038/s41592-019-0686-2

Vrard, M., Mosser, B., & Samadi, R. 2016, A&A, 588, A87, doi: 10.1051/0004-6361/201527259

Woudenberg, H. C., & Helmi, A. 2024, A&A, 691, A277, doi: 10.1051/0004-6361/202451743

Yu, J., Casagrande, L., Ciucă, I., et al. 2024, MNRAS, 530, 2953, doi: 10.1093/mnras/stae1091

Yu, J., Khanna, S., Themessl, N., et al. 2023, ApJS, 264, 41, doi: 10.3847/1538-4365/acabc8

APPENDIX

A. COST FUNCTION EVALUATION STEPS

1. **MESA Evolutionary Track:** For each iteration of the optimization, we first calculate a stellar model track using MESA version r22.05.1 (B. Paxton et al. 2011, 2013, 2015, 2018, 2019; A. S. Jermyn et al. 2023) using a set of model parameters (M_0, Y_0, $f = Z_0/X_0$, and $\alpha_{\rm mlt}$) determined by the differential evolution algorithm. The initial mass, initial helium mass abundance, initial metal mass abundance divided by initial hydrogen mass abundance, and convective mixing length, are varied in the following ranges, $0.75 \leq M_0 \leq 1.0$, $0.245 \leq Y_0 \leq 0.27$, $0.0001 \leq f \leq 0.003$, and $1.6 \leq \alpha_{\rm mlt} \leq 2.0$. The model element mixtures are enhanced in α-elements from their GS98 values (N. Grevesse & A. J. Sauval 1998) according to the values from M. N. Ishigaki et al. (2012), and are computed using correspondingly α-element enhanced opacities.

   Elemental diffusion is incorporated (A. A. Thoul et al. 1994), along with a small amount of exponential convective overshoot underneath the convective envelope ($f_{\rm ov,\,exp} = 0.01$ and $f_0 = 0.0005$). Overshoot is applied because most current models of low mass giant stars do not reproduce the observed location of the red giant branch luminosity bump, and incorporating envelope overshoot helps to resolve this discrepancy (M. Alongi et al. 1991; S. Khan et al. 2018; C. J. Lindsay et al. 2022). All models use a varying Eddington gray atmospheric boundary condition, and the mixing length prescription of (J. P. Cox & R. T. Giuli 1968).

   Along the stellar model's evolution, we save the stellar structure files along the part of the evolutionary track which coincides well with the target star's temperature and luminosity (within 10 σ from the values in Table 1). In order to perform asteroseismic modeling, mode frequencies must be calculated for all the models one would like to compare with the observations. In order to save time during the optimization process, we only calculate mode oscillation frequencies for these models which show good agreement with the values from M. N. Ishigaki et al. (2012).

2. $\boldsymbol{\chi^2_{\rm spectroscopic}}$**:** $\chi^2_{\rm spectroscopic}$ is calculated by comparing the model effective temperature, luminosity, and [Fe/H] to the literature values for HD 175305 and HD 128279 listed in Table 1. The overall $\chi^2_{\rm spectroscopic}$ is calculated as:

   $$\chi^2_{\rm spectroscopic} = \chi^2_{\rm Luminosity} + \chi^2_{\rm Temperature} + \chi^2_{\rm [Fe/H]} \tag{A1}$$

   with each spectroscopic parameter, P's, corresponding χ^2_P value calculated as:

   $$\chi^2_P = \frac{(P_{\rm obs} - P_{\rm model})^2}{\sigma^2_{P_{\rm obs}}}. \tag{A2}$$

3. **Calculate Model Mode Frequencies and** $\boldsymbol{\chi^2_{\rm seismic}}$**:** We then calculate the $\ell = 0$, 1, and 2 oscillation frequencies for the models along the evolutionary track with low values of $\chi^2_{\rm spectroscopic}$ using the stellar oscillation code GYRE (R. H. D. Townsend & S. A. Teitler 2013). We do this in steps, first calculating the $\ell = 0$ p-mode frequencies for all models with $\chi^2_{\rm spectroscopic} < 100$. For models with $\ell = 0$ mode frequencies which are a good match to the observed $\ell = 0$ modes, we calculate the $\ell = 2$ p-modes as well as the $\ell = 1$ mixed-modes following the mode isolation construction of J. M. J. Ong & S. Basu (2020).

   We match each model $\ell = 0$ of $\ell = 2$ p-mode frequencies to the observed frequencies based on their inferred values of radial order $n_{\rm p}$. We infer the observed modes' n_p values by plugging in the observed mode frequencies ($\nu_{\rm obs}$) and the observed $\Delta\nu$ to the rearranged asymptotic expression for p-mode frequencies, $n_{\rm p} = (\nu_{\rm obs}/\Delta\nu) - (\ell/2)$. The model $n_{\rm p}$ values are returned from GYRE. Since multiple $\ell = 1$ mixed-modes can have the same $n_{\rm p}$ value, we match the observed and model $\ell = 1$ modes using a nearest-neighbor search.

   Before calculating $\chi^2_{\rm seismic}$, the model mode frequencies must be corrected for the 'surface term,' which is a frequency-dependent frequency offset between models and stars caused by our inability to model the near-surface layers of a star properly. The $\ell = 0$ and 2 modes are corrected for the surface term using the two-term prescription from W. H. Ball & L. Gizon (2014), with the $\ell = 0$ modes used to determine the coefficients of the two-term surface correction. The $\ell = 1$ mixed modes must be treated differently, as the g-mode component of a mixed mode does not suffer from a surface effect as these modes do not reach the surface like p-modes do. We compute the $\ell = 1$ pure-p- and g-mode frequencies, and associated coupling matrices using the π/γ isolation method of J. M. J. Ong & S. Basu (2020). The surface term correction is applied only to the π-mode component of the mixed mode, and the surface-term-corrected mixed mode frequencies are determined using the corrected π-mode frequencies (see also the methods section of C. J. Lindsay et al. 2024).

With the surface corrected mode frequencies, the seismic χ^2 per degree of freedom, χ^2_{seismic}, is calculated for models along each evolutionary track as:

$$\chi^2_{\text{seis}} = \frac{1}{N_\nu - 1 - 2} \sum_{n}^{N_\nu} \frac{(\nu_{\text{obs},n} - \nu_{\text{model},n})^2}{\sigma^2_{\nu_{\text{obs},n}}}. \tag{A3}$$

with the total number of modes N_ν and with each observed mode frequency, $\nu_{\text{obs},n}$, and corresponding mode error $\sigma^2_{\nu_{\text{obs},n}}$, matched to the corresponding model mode frequency, $\nu_{\text{model},n}$.

4. **Account for limitations involved with correcting model frequencies using a power-law based frequency shift:** In the previous step, surface-term corrected frequencies are compared with the observed mode frequencies to find χ^2_{seismic}, however we need to account for models that are not good fits but appear to match the observed frequencies due to surface term corrections. Near surface modeling errors cause higher frequency model modes to be larger the corresponding mode frequencies, and this frequency difference increases at higher frequencies. To ensure the cost function prefers models with better fits we follow S. Basu & A. Kinnane (2018), J. M. J. Ong et al. (2021), M. S. Cunha et al. (2021), and C. J. Lindsay et al. (2024) in accounting for this by adding another penalty function to χ^2_{seis} calculated from the 2 lowest frequency radial and quadrupole modes.

$$\chi^2_{\text{low }n} = \sum_{\ell\in\{0,2\}} \frac{1}{2} \sum_{n=0}^{1} \left(\frac{\nu_{\text{obs},n} - \nu_{\text{model},n}}{\sqrt{\sigma^2_{\nu_{\text{obs},n}}}} \right)^2. \tag{A4}$$

To account for surface corrections which are too large, we compare the frequency difference between the uncorrected and corrected model mode frequencies (at ν_{max} to the frequency difference predicted using the RGB sample in Y. Li et al. (2023). The model surface correction frequency difference ($\delta\nu_{\text{actual}}$) at ν_{max} is found by interpolating over the model corrected and uncorrected frequencies while the predicted surface correction frequency difference from Y. Li et al. (2023) ($\delta\nu_{\text{predicted}} = a \cdot (g/g_\odot)^b \cdot (T_{\text{eff}}/T_{\text{eff},\odot})^c \cdot (d \cdot [\text{M/H}] + 1)$) depends on the models' surface gravity, effective temperature, and metallicity. $\chi^2_{\text{Surface Term}}$ was then calculated as

$$\chi^2_{\text{Surface Term}} = \frac{1}{10} \frac{(\delta\nu_{\text{actual}} - \delta\nu_{\text{predicted}})^2}{\sigma^2_{\delta\nu_{\text{predicted}}}}. \tag{A5}$$

with the error, $\sigma_{\delta\nu_{\text{predicted}}}$ calculated by finding the standard deviation of 500 $\delta\nu_{\text{predicted}}$ determinations using different values of the a, b, c, and d parameters, sampling based on the reported errors for the a, b, c, and d giant star parameters in Y. Li et al. (2023).

5. **Return χ^2_{total}:** The sum of each models' $\chi^2_{\text{spectroscopic}}$, χ^2_{seismic}, $\chi^2_{\text{low }n}$, and $\chi^2_{\text{Surface Term}}$ is then taken to be χ^2_{total}, and the best-fit model along the evolutionary track is taken to be the model with the lowest χ^2_{total}. That lowest χ^2_{total} value is the output of the cost function which the differential evolution algorithm is minimizing, and used to choose subsequent combinations of input model parameters. After one cost function evaluation finishes, the process starts again with a new MESA evolutionary track.